American Mineralogist, Volume 106, pages 964–982, 2021

Synthesis and characterization of Fe(III)-Fe(II)-Mg-Al smectite solid solutions and implications for planetary science

Valerie K. Fox[1,*], Robert J. Kupper[2], Bethany L. Ehlmann[1,3], Jeffrey G. Catalano[2], Joseph Razzell-Hollis[3], William J. Abbey[3], Dirk J. Schild[1], Ryan D. Nickerson[2], Jonas C. Peters[1], Sydney M. Katz[2,†], and Annabelle C. White[2]

[1]California Institute of Technology, 1200 E. California Boulevard, Pasadena, California 91125, U.S.A.
[2]Washington University in St. Louis, 1 Brookings Drive, CB 1169, St. Louis, Missouri 63130, U.S.A.
[3]NASA Jet Propulsion Laboratory, 4800 Oak Grove Drive, Pasadena, California 91109, U.S.A.

Abstract

This study demonstrates the synergies and limits of multiple measurement types for the detection of smectite chemistry and oxidation state on planetary surfaces to infer past geochemical conditions. Smectite clay minerals are common products of water-rock interactions throughout the solar system, and their detection and characterization provides important clues about geochemical conditions and past environments if sufficient information about their composition can be discerned. Here, we synthesize and report on the spectroscopic properties of a suite of smectite samples that span the intermediate compositional range between Fe(II), Fe(III), Mg, and Al end-member species using bulk chemical analyses, X-ray diffraction, Vis/IR reflectance spectroscopy, UV and green-laser Raman spectroscopy, and Mössbauer spectroscopy. Our data show that smectite composition and the oxidation state of octahedral Fe can be reliably identified in the near infrared on the basis of combination and fundamental metal-OH stretching modes between 2.1–2.9 μm, which vary systematically with chemistry. Smectites dominated by Mg or Fe(III) have spectrally distinct fundamental and combination stretches, whereas Al-rich and Fe(II)-rich smectites have similar fundamental minima near 2.76 μm, but have distinct combination M-OH features between 2.24 and 2.36 μm. We show that with expanded spectral libraries that include intermediate composition smectites and both Fe(III) and Fe(II) oxidation states, more refined characterization of smectites from MIR data is now possible, as the position of the 450 cm^{-1} absorption shifts systematically with octahedral Fe content, although detailed analysis is best accomplished in concert with other characterization methods. Our data also provide the first Raman spectral libraries of smectite clays as a function of chemistry, and we demonstrate that Raman spectroscopy at multiple excitation wavelengths can qualitatively distinguish smectite clays of different structures and can enhance interpretation by other types of analyses. Our sample set demonstrates how X-ray diffraction can distinguish between dioctahedral and trioctahedral smectites using either the (02,11) or (06,33) peaks, but auxiliary information about chemistry and oxidation state aids in specific identifications. Finally, the temperature-dependent isomer shift and quadrupole splitting in Mössbauer data are insensitive to changes in Fe content but reliability differentiates Fe within the smectite mineral structure.

Keywords: Smectites, clay mineralogy, reflectance spectroscopy, XRD, Raman spectra, Mars, planetary science

Introduction

Smectite clay minerals are among the most common products of water-rock interactions detected throughout the solar system and are key indicators of the geochemistry, oxidation state, and extent of aqueous activity in the environment in which they formed (Gates 2005; Bishop et al. 2008a; Ehlmann et al. 2011; Catalano 2013; Michalski et al. 2015; Gainey et al. 2017; Bristow et al. 2018). Tracing the history of aqueous alteration is a crucial aspect of understanding the formation and evolution of planetary bodies and water reservoirs throughout the solar system. Smectites are 2:1 layer phyllosilicates, comprised of an octahedral sheet between two Si(Al)-O tetrahedral sheets with an expandable interlayer, which contains H_2O and exchangeable cations that balance charge of the overall structure. A generalized formula is $(Ca,Na)_{0.3–0.5}(Fe,Mg,Al)_{2–3}(Si,Al)_4O_{10}(OH)_2 \cdot nH_2O$. Occupancy of the octahedral sheet is used to classify smectite minerals: trioctahedral smectites have all octahedral sites filled and are dominated by +2 cations; dioctahedral smectites have two of three octahedral sites filled and are dominated by +3 cations. There are several major end-member species, including dioctahedral nontronites [Fe(III)-rich], montmorillonites, and beidellites (Al-rich), and trioctahedral saponites [Mg- or Fe(II)-rich].

On Mars, smectite-bearing outcrops have been detected on the surface by orbital infrared instruments (Poulet et al. 2005, 2008; Bibring et al. 2006; Bishop et al. 2008a; Ehlmann et al. 2011; Carter et al. 2013; Ehlmann and Edwards 2014) and have also been investigated in situ by both the MER Opportunity

* Present address: University of Minnesota, John T. Tate Hall, 116 Church Street SE, Minneapolis, MN 55455-0149, U.S.A. E-mail: vfox@umn.edu
† Present address: Department of Aeronautics and Astronautics, Stanford University, Stanford, CA 94305, U.S.A.

rover (Arvidson et al. 2014; Fox et al. 2016) and the Mars Science Laboratory (MSL) Curiosity rover (Vaniman et al. 2013; Grotzinger et al. 2014; Bristow et al. 2015, 2018; Rampe et al. 2017). Fe- and Mg-bearing smectites are the most common phyllosilicates detected on Mars and are found in most exposures of ancient crust, suggesting early conditions conducive to silicate weathering or hydrothermal alteration (Poulet et al. 2005; Bishop et al. 2008a; Ehlmann et al. 2011; Carter et al. 2013; Catalano 2013; Ehlmann and Edwards 2014; Michalski et al. 2015). Fe- and Mg-bearing phyllosilicates, including smectites, are also found in carbonaceous chondrite meteorites and detected on other altered solar system bodies such as Ceres, C-class asteroids, and comets (Bunch and Chang 1980; Rivkin et al. 2003, 2006; De Sanctis et al. 2015; Ammannito et al. 2016). Due to their ubiquity and geochemical sensitivity to their formation environment, Fe- and Mg-bearing smectites are a key target material in planetary exploration in seeking to understand the aqueous history of the solar system. Their composition, along with Fe oxidation state, can be indicative of the aqueous conditions that altered the host material to the clay, if the properties can be discerned.

A wide range of smectites are observed on Earth with aluminous smectites (montmorillonite, beidellite) found most extensively in continental settings because of alteration of the predominantly felsic continental crust (Fig. 1). Nontronites and a wide range of intermediate Fe/Mg smectites are observed in oceanic settings and continental settings with basaltic rocks. Smectites formed in subsurface settings contain substantial ferrous [Fe(II)] iron rather than the typical ferric [Fe(III)] smectites

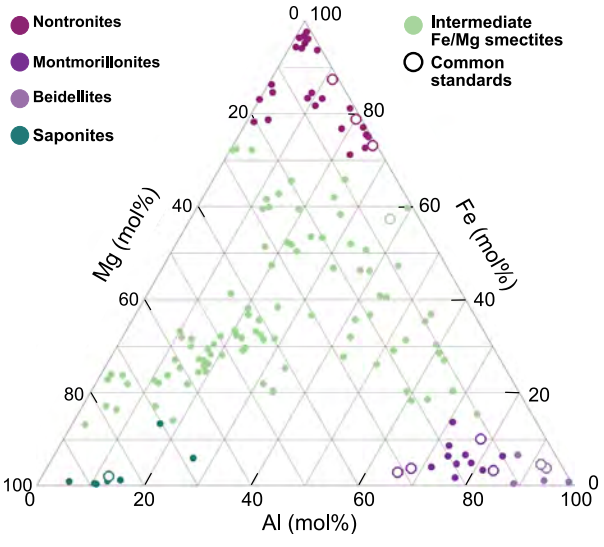

Figure 1. Terrestrial continental and marine smectite clay minerals span a wide range of bulk compositions (April and Keller 1992; Besson and Tchoubar 1972; Castellini et al. 2017; Curtis 1976; Daynyak et al. 1981; Desprairies et al. 1989; Gates 2005; Gaudin et al. 2004; Inoue and Utada 1991; Kimbara and Honda 1975; Kodama et al. 1988; Koster et al. 1999; Mermut and Cano 2001; Niu and Yoshimura 1996; Parthasarathy et al. 2003; Post 1984; Schmidt and Heystek 1953; Son et al. 2001; Suquet et al. 1975; Van Olphen and Fripiat 1979; Vantelon et al. 2003; Weir and Greene-Kelly 1962). Common smectite spectral standard samples are highlighted as open circles; Fe in these standards is predominantly in the 3+ oxidation state.

that form in soils, terrestrial sediments, and on the ocean floor where dissolved O_2 is abundant. The crusts of planetary bodies are generally dominated by rocks of mafic and ultramafic compositions, and most non-terrestrial bodies also lack an oxidizing atmosphere. Indeed, some have postulated the early Martian atmosphere was anoxic, and there is widespread evidence for Earth's anoxic early atmosphere (Catling and Moore 2003; Catalano 2013; Sholes et al. 2017). Consequently, Fe/Mg smectites of intermediate composition, containing Fe(II), Fe(III), or mixtures of the two, are expected to be common products forming on such bodies (Guven 1988; Burns 1993).

A few well-characterized smectite samples from terrestrial deposits, particularly from the Clay Mineral Society Special Clays, have found widespread use as spectral standards for identifying mineral phases on planetary bodies (Michalski et al. 2006; Bishop et al. 2008b; Treiman et al. 2014). The Al smectites (montmorillonites, beidellites) and end-member Fe(III) smectites (nontronites) are well-represented; a relatively limited compositional range of Mg smectites is represented by one common saponite standard. However, there is a large compositional range, representing Fe- and Mg-rich di- and tri-octahedral smectites that form from terrestrial alteration, for which there are no common standards (Fig. 1). In addition, while Fe(III)-bearing smectites (nontronites and also montmorillonites with moderate Fe contents) are well characterized, smectites containing Fe(II) or mixtures of Fe(II) and Fe(III) are poorly described because they are unstable against oxidation in air (Kohyama et al. 1973; Badaut et al. 1985; Guven 1988; Lajarige et al. 1998).

There has been significant effort to characterize the structural behavior as composition varies along binary axes by synthesizing smectites with controlled compositions and octahedral cation proportions. The Fe(III)-Mg (nontronite-saponite) series is a true solid solution in the absence of Al (Grauby et al. 1994), as is the Fe(III)-Al (nontronite-beidellite) series (Petit et al. 2015). The Al-Mg series (beidellite-saponite) is found to have an immiscibility gap that averages out in bulk measurements due to variability in the molecular structure within a clay particle (Grauby et al. 1993). There have been limited studies of native Fe(II)-bearing smectites, primarily trioctahedral in nature, and the impacts of oxidation on their structures (Chemtob et al. 2015, 2017). The substantial body of work on chemically reduced dioctahedral smectites that originally contained Fe(III) are instructive but of uncertain value to the present work, as such transformations result in dihydroxylation, perturbed layer charge, and rearrangement of octahedral cations (Manceau et al. 2000a, 2000b; Hadi et al. 2013) that would not occur in smectite natively occurring in the ferrous state. Laboratory synthesis studies also constrain physical conditions, such as temperature and pH, that control cation solubility into the smectite structure along binary solutions (Decarreau et al. 2008; Andrieux and Petit 2010).

The ability to determine the conditions in which a smectite mineral formed, including the aqueous geochemistry and oxidation state and by proxy the potential for habitability, is limited by the ability to accurately identify and measure smectite composition and mineral assemblages. Detailed characterization of the full compositional range of smectite minerals using techniques analogous to those employed in planetary exploration will help improve these capabilities for identification and compositional quantification. Here, we synthesize and report on the spectroscopic properties of a

suite of smectite samples that span the intermediate compositional range between Fe, Mg, and Al end-member species, including both Fe(III)- and Fe(II)-dominated samples, using bulk chemical analyses, X-ray diffraction, Vis/IR reflectance spectroscopy, UV and green-laser Raman spectroscopy, and Mössbauer spectroscopy. All spectra and patterns are available in the Online Material[1].

Methods

Smectite synthesis

Synthetic smectites were produced at Washington University using a hydrothermal sol-gel method modified from previous studies (Decarreau and Bonnin 1986; Chemtob et al. 2015). Solutions of magnesium, aluminum, iron(III), and iron(II) chlorides as well as sodium silicate were prepared from ultrapure deionized water (>18.2 MΩ cm). These solutions were mixed in stoichiometric proportions corresponding to the target smectite composition. Mg, Al, and Fe(II/III) solutions were mixed first as these are acidic in nature, followed by the addition of the alkaline sodium silicate solution. Upon mixing, these solutions quickly precipitated a gel, which were then aged for 24 h and centrifuged for 30 min at 16 500 RPM in sealed tubes. The supernatant fluid was removed, and the gel was resuspended in ultrapure water and centrifuged again to remove excess salt. The gel was again resuspended in ultrapure water, and the pH was adjusted to 9 using hydrochloric acid or sodium hydroxide. All steps in syntheses involving Fe(II) were conducted in an anaerobic chamber (Coy Laboratory Products) filled with a 97% N_2/3% H_2 mixture and a catalyst system that decomposes O_2 using the excess hydrogen in the chamber.

After pH adjustment, the gel suspensions were placed into PTFE-lined Parr acid digestion vessels and heated in an oven at 200 °C for 15 days. To prevent oxidation during heating, the syntheses involving Fe(II) were heated in a vacuum oven backfilled with ultrahigh-purity nitrogen gas. After cooling to room temperature, the smectites were immersed in a 0.5 M calcium chloride solution for several hours to Ca-saturate the interlayer via cation exchange, before being washed once more with ultrapure water and dried in a vacuum desiccator. Some of the Fe(III)-bearing samples were incompletely dried, such that during subsequent storage for ~12 months, some samples formed minor calcite impurities. These growths were identified by comparing X-ray diffraction (XRD) patterns collected before and after storage. We attribute the calcite impurities to CO_2(g) taken up by the excess water in the samples reacting with interlayer Ca during gradual dehydration during storage. These calcite impurities were removed by suspending the sample for 30 min in a pH 5 sodium acetate-acetic acid solution at 80 °C (Ulery and Drees 2008). Following this treatment, the smectites were again Ca-saturated, washed, and dried.

Chemical analysis

Elemental abundances were determined using ~50 mg of each synthetic smectite. These were first gently crushed with an agate mortar and pestle and added to a graphite crucible with 350 mg of lithium metaborate flux. The mixture was fused into a glass bead by heating in a muffle furnace at 1050 °C for 15 min. The glass beads were dissolved in 40 mL of 10% nitric acid, followed by a 1:100 dilution in 2% nitric acid. The diluted samples were analyzed by inductively coupled plasma optical emission spectroscopy (ICP-OES) using a Perkin Elmer Optima 7300DV instrument.

Structural formulas for the smectites were constructed by taking the molar abundances of each of the cations and normalizing their total positive charge against the 22 units of negative charge in the half-unit-cell formula. All Ca and Na is assigned to the interlayer. All Si is then assigned to the tetrahedral sheet, as is additional Al to bring the tetrahedral sheet to full occupancy at 4 atoms per half-unit-cell. For select Fe(III)-rich samples, Al is insufficient to fill the tetrahedral sheet and Fe(III) is then used to provide full occupancy. The remaining Al, Fe, and Mg are then assigned to the octahedral sheet. For the samples containing Fe(II), past syntheses have shown that minor Fe(II) oxidation may occur because of the difficulty in preventing any exposure to air during brief transfers between an anaerobic chamber and vacuum oven. The fraction of iron in the ferrous form [Fe(II)/total Fe] was determined by digestion of a subsample in 10 g/L ammonium bifluoride followed by complexation of Fe(II) by 1,10-phenanthroline (Tarafder and Thakur 2013). The Fe(II) concentration was then determined by measuring the absorbance at 510 nm using an ultraviolet-visible spectrophotometer (Thermo-Scientific Evolution 60). These assays were only performed for syntheses involving Fe(II), as the Fe(III) syntheses products at no point were exposed to chemical reductants.

X-ray diffraction

Powder XRD patterns were collected on a Bruker D8 Advance diffractometer equipped with a LynxEve XE energy-dispersive strip detector. Samples were gently ground in an agate mortar and pestle and placed into a silicon zero background sample holder for measurement. Samples containing Fe(II) were also enclosed in an air-tight dome to prevent oxidation during measurements, although this produced a large scattering feature between ~8° and 18° 2θ. Data were collected using Cu$K\alpha$ radiation (40 kV, 40 mA) from 3° to 65° 2θ with a 0.015° step size and a 0.8 s collection time per step. A continuous scanning data collection mode was employed with the total counts at each data point representing the sum of the counts measured as each of the 192 strips of the detector were swept through the corresponding 2θ position, yielding a total counting time per point of 153.6 s.

The XRD data were analyzed for both peak positions and lattice parameters, as the asymmetric nature of the turbostratic scattering bands make structural analysis from peak positions alone inaccurate (Moore and Reynolds 1997). The positions of the (001), (02,11), and (06,33) peaks were determined using least squares fitting of a single pseudo-Voigt profile and a linear background. Lattice parameter refinements were conducted using the Profex interface (Doebelin and Kleeberg 2015) to BGMN (Bergmann et al. 1998). This employed the approach of Ufer et al. (2004) to simulate the smectite X-ray scattering pattern, with the structure modified to match the compositions determined by sample digestion. The *c* lattice parameter was obtained through refinement to the (001) feature between 3° and 8° 2θ. For the in-sheet lattice parameters, a hexagonal sheet symmetry was assumed, fixing $a = b/\sqrt{3}$. The (02,11) and (06,33) bands were fit separately, from 18° to 21.5° 2θ and 57° to 64° 2θ, respectively. *b* lattice parameters are thus reported for each peak refinement. Corresponding *d*-spacings associated with diffraction features were then calculated from both the lattice parameters and peak positions for comparison. For the latter, the weighted average wavelength of 1.5418 Å for Cu$K\alpha_{1,2}$ radiation was used. This wavelength, along with 1.7903 Å for Co$K\alpha_{1,2}$, was used for peak position conversions between common X-ray tube wavelengths.

Visible to near-infrared spectroscopy

Visible/near-infrared reflectance (VNIR) spectra were acquired at wavelengths from 350 to 2500 nm and a spectral resolution of 6 nm using an Analytical Spectral Devices (ASD) Fieldspec3 with a 5° field of view and a custom goniometer device at Caltech. The samples were illuminated using a halogen light source placed at a 30° angle, and the fiber optic was positioned normal to the sample surface. The collected samples were calibrated by making measurements relative to a NIST-certified spectralon reflectance standard and correcting for its known properties. The bidirectional reflectances in the Online Materials[1] can thus be considered absolute reflectances. Samples were ground and sieved to particulate sizes <120 μm to reduce shadowing effects from larger grains sizes. Fe(II)-bearing samples were measured in a dry Ar atmosphere within an anoxic glove box.

Mid-infrared spectroscopy

Mid-infrared diffuse reflectance spectra were acquired on a Thermo-Scientific Nicolet iS50 transform infrared spectrometer with a 4 cm^{-1} sampling interval and averaged 512 scans. Fe(III)-bearing samples were placed in a dry air-purged sample chamber to acquire diffuse reflectance measurements over 5000–400 cm^{-1} (2–25 μm). The system was purged with dry N_2 during measurements of the Fe(II)-bearing samples. The system was calibrated using a rough Al target, which was assumed to have a reflectance of unity. (Any investigations requiring absolute reflectance and utilizing the Online Materials[1] should scale MIR to Vis/NIR data values.)

Each sample was also measured using the SensIR Durascope attenuated total reflectance accessory on a Nicolet Magna 860 Fourier transform infrared spectrometer. Powdered samples were pressed against a diamond crystal, and spectra were acquired over 4000–400 cm^{-1} (2.5–25 μm) using a KBr beam splitter and an uncooled triglycine sulfate detector with a KBr window. Background calibration spectra were acquired using the diamond crystal alone. All samples were measured in air, as oxidation during the short integration times (<3 min) is considered negligible, and the sample size required is small.

Raman spectroscopy

Raman patterns were collected on loosely packed powdered samples on a Renishaw M1000 micro-Raman spectrometer using a 532 nm solid-state 100 mW laser with a 2400 nm diffraction grating on loosely packed powdered sample and a spot size of 100 μm. The laser power was attenuated to 10% to avoid ablating the samples, and scans were averaged to improve counting statistics. Spectra were collected between 100 and 4000 cm^{-1} with a 1 cm^{-1} sampling interval. Wavelength accuracy was

calibrated using a silicon chip to within 0.5 cm^{-1}. Spectra were background corrected using a cubic spline interpolation. All samples were measured in air. Exposure of the Fe(II) samples was minimized prior to measurement, and oxidation during the <8 min exposure times is considered minimal. The 532 nm excitation wavelength is equivalent to the Raman spectrometry system planned for the SuperCam instrument designed for the Mars 2020 rover mission (Wiens et al. 2017).

Deep-ultraviolet (DUV) Raman spectra were obtained using Mineralogy and Organic Based Investigations Using Ultraviolet Spectroscopy (MOBIUS), the laboratory prototype for the Scanning Habitable Environments with Raman and Luminescence for Organics and Chemicals instrument (SHERLOC) designed for the Mars 2020 rover mission (Beegle et al. 2017). Measurements were done using a 248.58 nm pulsed laser (Photon Systems, Inc) with a focused spot diameter of ~40 µm, an 1800 lines/mm diffraction grating and a Horiba Symphony e2v 42-10 CCD liquid nitrogen cooled (–140 °C) detector. Each spectrum was acquired over 30 s at a pulse rate of 40 Hz, totaling 1200 pulses. Spectra were collected between over 1024 points between ~570 and ~4200 cm^{-1} with a spectral accuracy of 3.8 cm^{-1}, and wavelengths were calibrated using validating the position of the primary and secondary laser lines at 248.58 and 252.93 nm, respectively. For each sample of loosely packed powder, 25 spectra were obtained in a 5×5 array with a spacing of 100 µm. Cosmic rays were identified as outliers in the distribution of intensity values in each Raman shift channel and replaced by the value of adjacent points (Uckert et al. 2019). Further processing was done by in-house Python scripts utilizing publicly available packages Numpy, SciPy, and LMFIT (van de Walt et al. 2011; Jones et al. 2001; Newville et al. 2014). Processing included subtraction of a linear baseline by least-squares regression, a recalibration of Raman shift values based on the position of the atmospheric N_2 peak relative to its literature position of 2331 cm^{-1}, and subsequent removal of atmospheric N_2 and O_2 peaks by subtraction of a standard atmospheric Raman spectrum acquired on the same spectrometer. The processed spectra were normalized with respect to the N_2 peak amplitude and peak positions, FWHM, and intensities were determined by fitting with Gaussian functions.

Mössbauer spectroscopy

Mössbauer spectra were recorded on a spectrometer from SEE Co. operating in the constant acceleration mode in a transmission geometry. Samples were ground in an agate mortar and, depending on the Fe content, 20–60 mg were added to 500 mg boron nitride and mixed in a glass vial to create a homogenous sample (Online Material[1] Table OM4). The resulting mixture was added to a Delrin cup, capped, and measured. Spectra were recorded with the temperature maintained using an SVT-400 Dewar from Janis. The quoted isomer shifts are relative to the centroid of the spectrum of a metallic foil of α-Fe at room temperature. Data analysis was performed using the program WMOSS (www.wmoss.org) and quadrupole doublets were fit to Voigt lineshapes.

Results and Discussion

Elemental abundance of synthesized smectites

Ten Fe(III)-bearing smectites and six Fe(II)-bearing smectites were synthesized with compositions intermediate to widely used standards (Fig. 2). In calculations of structural formulas (Table 1), Fe(III) was required to fill the tetrahedral sheet in the two most Fe(III)-rich compositions (samples A and B). Mg content was reduced relative to Fe and Al in each of the final compositions compared to the initial solution, matching observations of other smectite syntheses and suggesting higher Mg solubility than Fe or Al in this system (Chemtob et al. 2015). Octahedral occupancies per half-cell derived from the structural formula (Table 1) indicates that the Fe(III) smectites are generally dioctahedral in

Table 1. Calculated molecular formulas of synthetic intermediate smectite samples

Sample	Calculated formula	Octahedral occupancy	%Fe (II)[a]
A	$Ca_{0.37}Na_{0.10}[Fe^{III}_{1.68}Mg_{0.40}][Si_{3.32}Al_{0.51}Fe^{III}_{0.17}]O_{10}(OH)_2$	2.08	–
B	$Ca_{0.28}[Fe^{III}_{1.54}Mg_{0.64}][Si_{3.55}Al_{0.39}Fe^{III}_{0.06}]O_{10}(OH)_2$	2.18	–
C	$Ca_{0.35}Na_{0.22}[Fe^{III}_{1.24}Mg_{0.37}Al_{0.39}][Si_{3.43}Al_{0.57}]O_{10}(OH)_2$	2.00	–
D	$Ca_{0.35}Na_{0.23}[Fe^{III}_{1.04}Mg_{0.46}Al_{0.53}][Si_{3.44}Al_{0.56}]O_{10}(OH)_2$	2.03	–
E	$Ca_{0.40}[Fe^{III}_{1.06}Mg_{0.93}Al_{0.15}][Si_{3.70}Al_{0.30}]O_{10}(OH)_2$	2.14	–
F	$Ca_{0.35}Na_{0.07}[Fe^{III}_{0.96}Mg_{0.84}Al_{0.29}][Si_{3.80}Al_{0.20}]O_{10}(OH)_2$	2.09	–
G	$Ca_{0.24}[Fe^{III}_{0.69}Mg_{1.12}Al_{0.52}][Si_{3.66}Al_{0.34}]O_{10}(OH)_2$	2.33	–
H	$Ca_{0.39}[Fe^{III}_{0.68}Mg_{1.75}Al_{0.02}][Si_{3.60}Al_{0.40}]O_{10}(OH)_2$	2.45	–
I	$Ca_{0.31}Na_{0.28}[Fe^{III}_{0.57}Mg_{0.92}Al_{0.63}][Si_{3.67}Al_{0.33}]O_{10}(OH)_2$	2.12	–
J	$Ca_{0.37}[Fe^{III}_{0.27}Mg_{2.31}Al_{0.08}][Si_{3.60}Al_{0.40}]O_{10}(OH)_2$	2.66	–
K	$Ca_{0.23}[Fe^{II}_{2.23}Fe^{III}_{0.28}Al_{0.26}Mg_{0.12}][Si_{3.51}Al_{0.49}]O_{10}(OH)_2$	2.89	89.0
L	$Ca_{0.30}[Fe^{II}_{1.43}Fe^{III}_{0.23}Al_{0.40}Mg_{0.66}][Si_{3.55}Al_{0.45}]O_{10}(OH)_2$	2.72	86.0
M	$Ca_{0.29}Na_{0.05}[Fe^{II}_{1.50}Fe^{III}_{0.11}Al_{0.29}Mg_{0.92}][Si_{3.46}Al_{0.54}]O_{10}(OH)_2$	2.81	93.1
N	$Ca_{0.27}Na_{0.08}[Fe^{II}_{0.80}Fe^{III}_{0.09}Al_{1.29}Mg_{0.10}][Si_{3.54}Al_{0.46}]O_{10}(OH)_2$	2.28	90.0
O	$Ca_{0.28}Na_{0.12}[Fe^{II}_{0.64}Fe^{III}_{0.11}Al_{1.08}Mg_{0.50}][Si_{3.56}Al_{0.44}]O_{10}(OH)_2$	2.34	85.4
P	$Ca_{0.29}Na_{0.06}[Fe^{II}_{0.69}Fe^{III}_{0.11}Al_{0.35}Mg_{1.57}][Si_{3.57}Al_{0.43}]O_{10}(OH)_2$	2.72	86.6

[a] mol% of total iron occurring as Fe(II); only measured for syntheses involving iron(II) chloride.

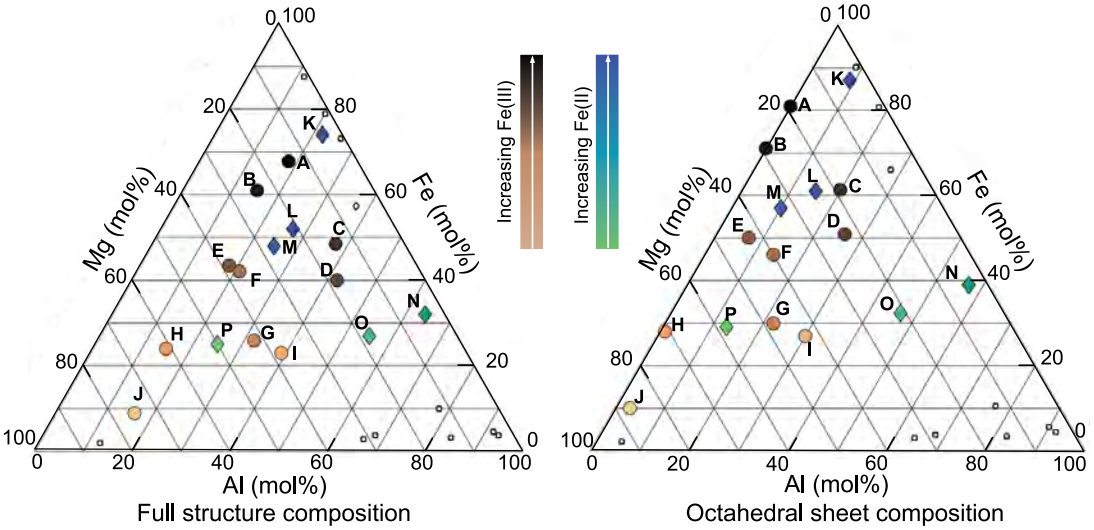

Figure 2. Ternary diagrams showing the compositions of 16 synthetic ferruginous smectite samples investigated in this study. The full structural composition is shown in the left diagram, whereas the right diagram shows the composition of the octahedral sheet only. Fe(III)-bearing samples are shown in brown circles. Fe(II)-bearing samples are shown in blue-green diamonds. Colors trend from light to dark with increasing octahedral Fe content. Colors are kept consistent in following figures. Small squares show the compositions of Clay Mineral Society standards NAu-1, NAu-2, Ng-1, SWa-1, Sap-Ca1, SWy-1, SAz-1, STx-1b, SCa-3, SBId-1 that are frequently used as spectroscopic standards (Van Olphen and Fripiat 1979; Post 1984; Gates 2005; Gailhanou et al. 2012; Castellini et al. 2017).

nature with the exception of samples G, H, and J, which have formulas suggestive of di-trioctahedral clays. Fe(II) smectite compositions suggest trioctahedral compositions similar to those studied by Chemtob et al. (2015), except for two Al-rich compositions (N and O). Samples K, L, M, and P are consistent with trioctahedral Fe(II)-Mg smectites, sample N is dioctahedral, and sample O is a di-trioctahedral smectite. Seven to 15% of the iron in the Fe(II) smectites oxidized during synthesis (Table 1), which is attributed to leakage of small quantities of O_2 into the vacuum oven during synthesis or from leakage into the anaerobic chamber during pre- or post-synthesis treatments.

X-ray diffraction

The XRD patterns (Fig. 3) of the synthesized clays confirm that all are smectites, with broad asymmetrical features that are indicative of turbostratic stacking. No other crystalline phases are present except for in sample L, which has <0.4 wt% quartz (determined by Rietveld refinement) which is attributed to contamination during sample preparation for XRD or present in the sample holder. The (001) diffraction peaks near 6° 2θ (Table 2) correspond to basal layer spacings between 13 and 17 Å (Table 3), consistent with 1 to 3 layers of water in the interlayer. Table 2 also shows the equivalent peak position for each feature if measured by Co*K*α radiation, as done onboard the Mars Science Laboratory CheMin XRD instrument. The relatively weak and broad (001) reflections are often observed in XRD patterns of synthetic smectites (Grauby et al. 1993, 1994; Chemtob et al. 2015) and indicate small coherent domain sizes, i.e., a small number of stacked layers per crystallite. The peak between 25 to 30° 2θ is primarily the (003) reflection, which like the (001) feature is broad because of the small coherent domain size (Fig. 3a). This feature also includes scattering from some water associated with the samples (Morgan and Warren 1938). The remaining features are (*hk*) peaks associated with X-ray scattering from within the smectite sheet (Brindley and Brown 1980; Moore and Reynolds 1997).

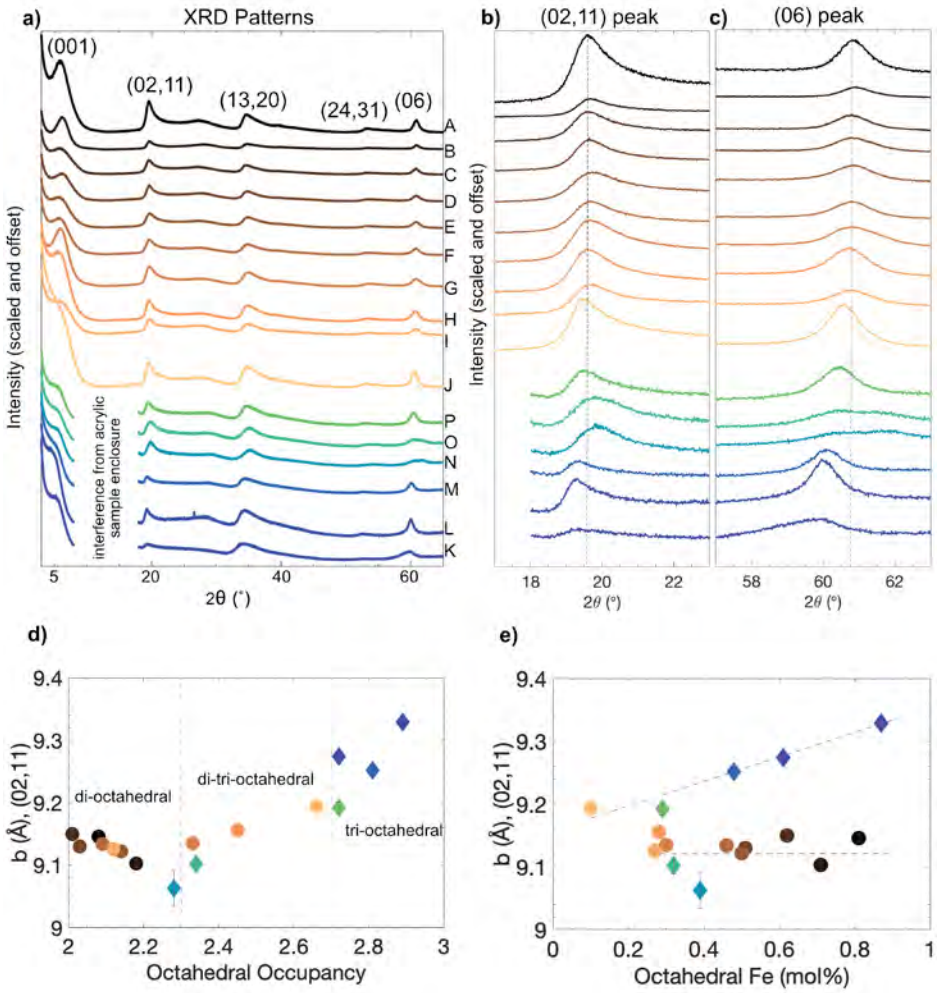

Figure 3. (**a**) XRD patterns of the synthetic smectite samples. No background subtraction is performed to avoid aliasing broad features. (**b**) Peak positions of the (02,11) peaks and (**c**) of the 060 peak shift to smaller angles with decreasing Fe(III) content. (**d**) The calculated b-axis spacing based on fitting the (02,11) peak with respect to octahedral occupancy; vertical lines delineate approximate distinctions between di-, di-tri-, and tri-octahedral structures. (**e**) Dioctahedral samples show little dependence of the *d*-spacing on octahedral iron content, although the trioctahedral Fe(II)-bearing samples show a more linear trend (trend lines fit only to the dioctahedral and trioctahedral samples, respectively).

TABLE 2. Measured peak positions of diagnostic diffraction features of the synthetic smectites using CuKα and their calculated corresponding positions for measurements using CoKα radiation

Sample	°2θ CuKα			°2θ CoKα		
	(001)	(02,11)	(06,33)	(001)	(02,11)	(06,33)
A	6.00(8)[a]	19.61(1)	60.856(8)	6.97	22.81	72.04
B	6.29(2)	19.71(1)	60.93(1)	7.30	22.93	72.14
C	5.99(8)	19.63(1)	60.800(9)	6.96	22.83	71.97
D	6.31(3)	19.64(1)	60.87(1)	7.33	22.84	72.06
E	6.04(6)	19.76(2)	60.843(8)	7.01	22.98	72.02
F	6.06(4)	19.71(1)	60.806(8)	7.04	22.93	71.98
G	6.10(1)	19.68(1)	60.86(2)	7.08	22.89	72.05
H	6.13(1)	19.63(1)	60.718(6)	7.12	22.83	71.87
I	6.51(2)	19.72(1)	60.807(9)	7.56	22.94	71.98
J	6.37(2)	19.50(1)	60.584(4)	7.40	22.68	71.70
K	5.36(5)	19.21(3)	59.37(2)[b]	6.22	22.35	70.20
L	5.2(1)	19.28(1)	60.019(8)	6.10	22.42	71.00
M	5.46(6)	19.32(2)	60.096(7)	6.34	22.47	71.10
N	5.7(1)	19.89(1)	61.13(4)[b]	6.63	23.13	72.38
O	5.6(1)	19.81(2)	60.84(3)[b]	6.51	23.04	72.01
P	5.7(9)	19.50(2)	60.42(1)	6.62	22.68	71.51

[a] Numbers in parentheses represent fitting uncertainties in the last digit.
[b] Peaks consist of doublets but fitted as single feature. When modeled as doublets, contain peaks at 58.32(14)° and 59.61(5)° for K, 60.42(12)° and 61.86(10)° for N, and 60.29(12)° and 61.65(18)° for O.

TABLE 3. Comparison between *d*-spacings as derived from the fitted lattice parameters and as calculated from observed peak positions

Sample	d_{001} (Å)		$d_{02,11}$ (Å)		$d_{06,33}$ (Å)	
	Lattice	Peak	Lattice	Peak	Lattice	Peak
A	14.9	14.7	4.57	4.53	1.526	1.522
B	14.2	14.0	4.55	4.50	1.524	1.520
C	14.6	14.7	4.58	4.52	1.528	1.523
D	14.0	14.0	4.57	4.52	1.526	1.522
E	14.8	14.6	4.56	4.49	1.527	1.522
F	14.7	14.6	4.57	4.50	1.528	1.523
G	14.7	14.5	4.57	4.51	1.526	1.522
H	14.6	14.4	4.58	4.52	1.530	1.525
I	14.0	13.6	4.56	4.50	1.528	1.523
J	13.0	13.9	4.60	4.55	1.533	1.528
K	16.5	16.5	4.66	4.62	1.552	1.557[a]
L	16.8	16.8	4.64	4.60	1.545	1.541
M	16.1	16.2	4.63	4.59	1.543	1.540
N	15.4	15.5	4.53	4.46	1.520	1.516[a]
O	15.5	15.8	4.55	4.48	1.525	1.523[a]
P	15.4	15.5	4.60	4.55	1.536	1.532

[a] Determined from position when fitting with a single peak. Fitting (06,33) bands as a double yield d-spacings of 1.582 and 1.551 Å for K, 1.532 and 1.500 Å for N, and 1.535 and 1.504 Å for O.

The (060) *d*-spacing, typically calculated from the peak position of the (06,33) band near 60° 2θ (Table 3; Fig. 3c), is most commonly used to determine unit-cell dimensions. This is also typically considered diagnostic of dioctahedral vs. trioctahedral structures, although, as our results show, there is overlap in the range of values for these features once the diversity of compositions is considered. The Fe(III) smectites in this study (samples A–J) have (060) *d*-spacings between 1.520 and 1.528 Å based on peak positions. The Fe(II) smectites show a much broader range, from 1.516 to 1.557 Å, consistent with prior work (Chemtob et al. 2015). Three of the Fe(II) smectites (K, N, and O) have splittings in the (06,33) peaks that suggest the presence of separate domains of distinct clay compositions intermixed among the layers, which has been observed to occur in previous syntheses of Fe(II) smectites (Chemtob et al. 2015), as well as other smectite compositions (Grauby et al. 1993). The shoulder feature for sample K may indicate an anomalously long *d*-spacing (~1.58 Å), but the exact origin of this feature is uncertain as the dome used to seal the sample also produce an increase in background scattering near this feature. The splittings in the (06,33) peak for samples N and O are clearer in nature and suggest mixtures of trioctahedral and dioctahedral domains. This parallels a miscibility gap previously reported for the Mg saponite-beidellite series (Grauby et al. 1993), suggesting that Fe(II) saponites also display such a gap as Al content increases. Peak positions of the (02,11) peak similarly show small variation among the Fe(III) smectites and much larger variations among the Fe(II) smectites (Table 2; Fig. 3b). The derived lattice spacing, as calculated from peak refinement, reflects octahedral coordination state (Fig. 3d). Dioctahedral sample basal spacings exhibit little dependence on Fe(III) octahedral content (Fig. 3e), but tri- and di-trioctahedrally coordinated samples demonstrate a more linear trend toward increasing *d*-spacing with increasing octahedral Fe [both Fe(II) and Fe(III)].

Lattice parameters were refined for both Fe(III) and Fe(II) smectites using a single smectite structure to model both the (02,11) and (06,33) peaks, and thus obtained one *b* value from each, even when peak splitting was observed (Table 3). Calculation of the (060) *d*-spacings from lattice parameters obtains values ~0.004 Å larger than values determined from peak positions (Table 4). This discrepancy is real and results from smectite sheets scattering as two-dimensional crystals, with peak positions occurring at slightly higher angles in 2θ than the actual (06,33) position (Brindley and Brown 1980; Moore and Reynolds 1997). Lattice parameter refinements of the (02,11) show similar trends in *b* values as the peak positions. However, the discrepancy between the *d*-spacing as derived from the peak position and the lattice parameter is an order of magnitude larger in this case, with peak positions underestimating actual *d*-spacings by 0.04 to 0.07 Å. While this is a long-established aspect of the X-ray scattering properties of turbostratic smectites, this is again emphasized here because the (02,11) peak is the primary structural features observable in X-ray diffraction patterns collected by the MSL rover, as the (06,33) peak is outside of the angular range of the instrument.

Visible to Near-Infrared spectroscopy

Spectral features in the Visible to Near Infrared (VNIR) wavelength region are caused by electronic absorptions related to charge transfer and crystal field splitting, as well as the overtones and combinations of the fundamental vibrational

TABLE 4. Lattice parameters derived from refinement to individual peaks assuming hexagonal sheet symmetry

Sample	*c* (Å)	*b* (Å), (02,11)	*b* (Å), (06,33)
A	14.87(12)[a]	9.146(7)	9.158(10)
B	14.18(3)	9.103(7)	9.147(11)
C	14.57(23)	9.150(8)	9.168(2)
D	14.04(18)	9.130(7)	9.154(5)
E	14.79(33)	9.122(7)	9.161(4)
F	14.72(21)	9.134(6)	9.167(5)
G	14.70(3)	9.135(3)	9.154(3)
H	14.61(19)	9.156(4)	9.179(2)
I	13.95(43)	9.126(9)	9.169(2)
J	13.02(16)	9.194(3)	9.197(2)
K	16.52(9)	9.329(4)	9.310(17)
L	16.80(12)	9.274(6)	9.268(3)
M	16.11(11)	9.252(10)	9.259(41)
N	15.39(10)	9.063(29)	9.119(15)
O	15.46(14)	9.102(13)	9.149(6)
P	15.35(12)	9.192(9)	9.217(2)

[a] Numbers in parentheses represent fitting uncertainties in the last digit.

modes of the chemical bonds within a mineral structure, such that the wavelength position of absorption features provides characteristic information about the mineral composition (Gates et al. 2017). The reflectance also depends on the particle size and viewing geometry of the samples under investigation. The VNIR reflectances of the synthetic smectite samples exhibit absorptions caused by electronic transitions in Fe(II) and Fe(III), and cation-OH bending and stretching modes between 0.5 and 2.5 μm (Fig. 4).

In the visible and short-wavelength near-infrared (0.4–1 μm), Fe crystal field absorptions dominate the spectral shape. Within the Fe(III) samples, overlapping ferric features dominate the spectrum between 0.4 and 1 μm, but vary as a function of Fe content. Fe(III)-bearing samples A–J all have a spectral maximum near 0.76 μm. The positive spectral slope from 0.4–0.76 μm observed in all Fe(III)-bearing samples is caused by charge transfer bands that are centered in the UV and the broad 0.60 and 0.96 μm absorptions, attributed to electron transitions in the Fe(III) ions in the octahedral structure (Hunt 1977). A narrower feature centered at 0.48 μm is also an Fe(III) charge transfer absorption (Rossman 1976; Hunt 1977). The 0.96 μm absorption is present in all samples save sample J, which only has 9% octahedral Fe(III). The 0.48 μm absorption is most pronounced in samples with relatively less Fe(III) content, which is consistent with an enhanced charge transfer absorption due to substitution of a 3+ ion into a 2+ crystal site (Burns 1970; Hunt 1977). The Fe(II)-bearing samples have a distinctly different spectral shape in the visible and near infrared due to Fe(II) electronic absorptions. Samples K–P have a spectral maximum at 0.5 μm, and very broad absorption features centered around 0.72, 0.88–0.92, and 1.11–1.13 μm, attributed to Fe(II) crystal field absorptions (Hunt 1977; Bishop et al. 2008b).

All samples have broad, asymmetrical absorptions centered at 1.91 μm, caused by the combination of bending and stretching modes of H_2O molecules within the mineral structure. The interlayer of smectite clays can accommodate significant molecular substitution, such that ambient humidity affects H_2O absorption into the mineral structure. The depth and structure of the 1.91 μm absorption feature is a function of the samples' hydration; a shoulder around 1.97 μm that occurs in some samples indicates the presence of relatively more absorbed water in the interlayer (Bishop et al. 1994). The combination of the symmetric and asymmetric stretch together with the H_2O bending mode occurs at 1.15 μm, and is detectable in the Fe(III)-bearing samples. Sample J, which has the least strong Fe electron features, also shows the second overtone of the H_2O stretching mode at 0.97 μm, which is obscured by the stronger Fe absorptions in the other samples. The 0.97 and 1.15 μm absorptions are not apparent in the Fe(II)-bearing samples, likely due to the stronger overlapping Fe(II) electronic features. All samples also exhibit a strong absorption centered near 1.41 μm due to the first overtone of the structural OH and H_2O, and a shoulder at 1.46 μm

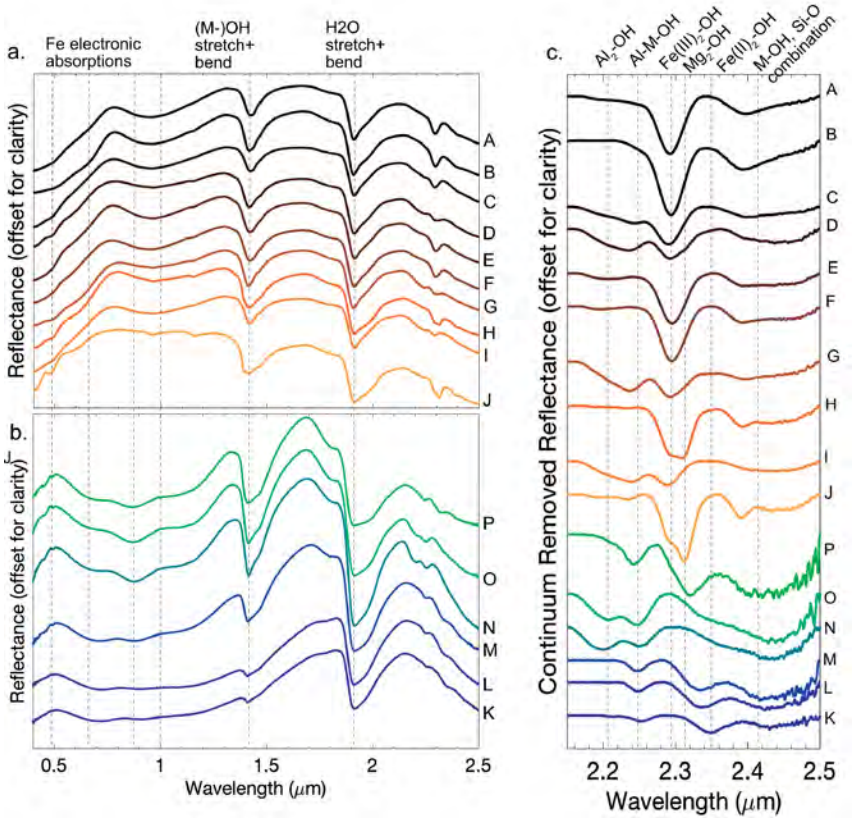

Figure 4. Visible to near infrared reflectance spectra of (**a**) Fe(III)-bearing smectite samples and (**b**) Fe(II)-bearing smectite samples. (**c**) Continuum removed absorption features between 2.1 and 2.5 μm for all samples with wavelengths of overtones and combination absorptions from the literature indicated as detailed in the text.

is attributed to a more H_2O-saturated interlayer (Bishop et al. 1994). Structure within this absorption is due to overtones of the Metal-OH (M-OH) stretching and bending modes observed at longer wavelengths. Samples H, J, and P, with the most octahedral Mg, have a band at 1.395 µm, compared to all other more Fe-rich samples that have absorptions centered toward 1.43 µm, consistent with prior work (Madejová et al. 2000).

The NIR region between 2.1 and 2.5 µm is particularly diagnostic of smectite clay composition because absorptions caused by the combination of the bending and stretching modes of the octahedral cations and hydroxyl molecules occur in this range. The intensities and center positions of these absorptions shift as a function of the relative abundance of Fe(III), Fe(II), Al, and Mg in the octahedral layer (Fig. 5). Samples with high octahedral Al contents show absorption features in the 2.20–2.25 µm range (Fig. 5a). In the Fe(III)-bearing samples C, D, H, and I, shallow and broad absorptions around 2.23 µm are combination absorptions attributable to Al-Fe(III)-OH and Al-Mg-OH bending and stretching modes. The Al-related absorptions are more well defined in the Fe(II)-bearing samples; a narrow absorption feature shifts from 2.25 µm in the most Fe(II)-rich samples to 2.23 µm in the Fe(II)-poor (Mg-rich) samples. Samples O and N, which are the most Al-rich samples in the suite, also have well-defined Al-Al-OH absorptions at 2.20 µm. All of the Fe(III)-bearing samples have distinct absorptions centered at 2.28 µm caused by the combination of the $Fe(III)_2$-OH bending and stretching vibrational modes that occur in the mid-infrared (Fig. 5b) (Madejová et al. 2000; Gates 2005). Samples H and J also have an absorption center at 2.31 µm attributed to the Mg-OH-Mg combination absorption (Grauby et al. 1994). Sample K has a dominant absorption at 2.35 µm attributed to $Fe(II)_2$-OH combination modes, and the position of this feature shifts to 2.33 µm in samples L and M as Fe(II) in the octahedral sheets decreases. Samples N and O lack a defined absorption feature in this wavelength range and have only a shallow shoulder near 2.33 µm. Sample P has an asymmetric absorption at 2.32, consistent with the low-Fe and high-Mg octahedral sheet content in this sample.

The Fe(III)-bearing samples have an absorption band that does not shift significantly as a function of composition at ~2.39 µm. It is most strongly defined in samples J, H, A, and B, but is detectable in all of the spectra. This feature is attributed to the combination of cation-OH stretches in the octahedral sheets and the tetrahedral Si-O stretch (Gates 2005). Mg-dominated samples H and J have a narrower, more pronounced absorption compared to the wider features in the more Fe(III)-dominated samples. The more aluminous samples, C, D, G, I, N, and O, together with all of the Fe(II)-bearing samples, have broad bands with centers shifted toward 2.45 µm. In the Fe(II)-bearing samples, this shift is approximately linear as a function of Mg content, although the Fe(III) samples do not show well-defined compositional dependence (Fig. 5c).

Mid-infrared spectroscopy

Attenuated total reflectance (ATR). The attenuated total reflectance (ATR) spectra of the suite of ferruginous smectites are shown in Figure 6, and assignments are made based on previous works. Peaks in the ATR spectra are primarily a function of the absorption coefficient of the material and peaks in the 400–4000 cm^{-1} range are caused by the fundamental molecular vibrational modes. Higher degrees of crystallographic symmetry sharpen peaks, whereas less-ordered structures and

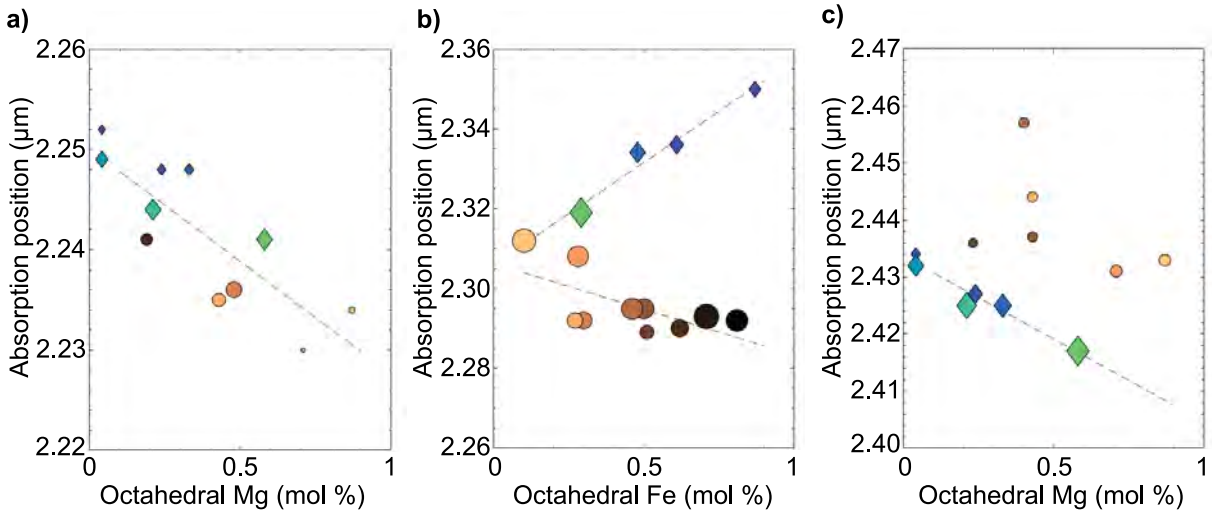

Figure 5. Trends in the position and intensity of metal-OH combination absorptions. Larger data points indicate greater relative band depth of the absorption, from 0.01–0.34, and are relative across panels. (**a**) Position of ~2.24 µm absorptions as a function of octahedral magnesium. Absorptions at shorter wavelengths (~2.235 µm) are attributed to Al-Mg-OH combination bands, whereas absorptions at longer wavelengths (~2.25 µm) are attributed to Al-Fe(II)-OH combination bands. The samples with the highest Fe(III) content have low Al content and therefore have negligible Al-M-OH absorptions. Trend line is fit to both Fe(II) and Fe(III) bearing samples that have a measurable absorption. (**b**) Position of the ~2.3 µm absorption as a function of octahedral Fe content. $Fe(II)_2$-OH combination modes trend toward 2.36 µm, whereas $Fe(III)_2$-OH combination modes trend toward 2.29 µm. Mg-M-OH combinations trend toward 2.31 µm. (**c**) Position of the ~2.45 µm absorption as a function of octahedral Mg content. This feature is broad and shallow in the Fe(III)-bearing samples, without a significant trend, but the Fe(II)-bearing samples demonstrate a linear trend toward shorter wavelengths with increasing octahedral Mg content.

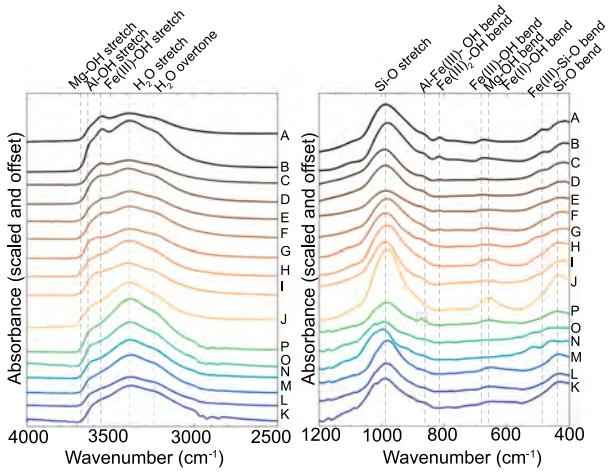

Figure 6. Attenuated Total Reflectance (ATR) spectra of the synthetic ferruginous smectite suite. (**a**) The hydroxyl bending modes and (**b**) the hydroxyl and tetrahedral stretching modes. Peak attributions are described in the text. The peak at ~850 cm^{-1} in the shaded box is attributed to calcite contamination in sample P.

overlapping vibrational modes produce broad peaks. Generally, octahedral OH stretching modes occur between 3800–3000 cm^{-1} (2.63–3.33 μm) (Fig. 6a), and the octahedral OH bending modes, together with the tetrahedral stretching and bending modes, occur between 1200–400 cm^{-1} (8.33–25 μm) (Fig. 6b).

All samples have well-defined features between 3800–3000 cm^{-1} (2.63–3.33 μm) that are caused by H_2O-related vibrational modes and cation-OH stretching modes. A shoulder feature that occurs 3220 cm^{-1} (3.1 μm) is the first overtone of the H_2O bending mode that occurs in all samples at 1635 cm^{-1} (6.12 μm) (Clark et al. 1990; Bishop et al. 1994; Madejová et al. 2002). A broad peak centered around 3390 cm^{-1} (2.94 μm) is attributed to outer-sphere H_2O bonding within the interlayer; its strength has been correlated with the hydration levels of the smectite (Bishop et al. 1994; Madejová et al. 1994), and its relative strength among samples measured here also tracks with observed trends in the near-infrared that suggest that some of the samples are more hydrated than others. Peak and shoulder features between 3700–3550 cm^{-1} (2.70–2.81 μm) are attributed to cation-OH stretching modes. Samples A–F have a peak feature, most clearly observed in samples A and B, at 3550 cm^{-1} (2.81 μm) that is associated with $Fe(III)_2$-OH stretching (Gates 2005). Samples I and J have a well-defined shoulder feature at 3680 cm^{-1} (2.71 μm) that is ascribed to the Mg_2-OH stretching vibration (Grauby et al. 1994). A shoulder at 3630 cm^{-1} (2.75 μm) is prominent in almost all of the samples and is the dominant feature in the Fe(II)-bearing samples (Fig. 6a). This is most consistent with features that have been attributed to Al_2-OH or Al-M-OH bending modes in other smectite samples (Grauby et al. 1993; Madejová et al. 1994; Gates 2005) and is likely the cause in these samples. The $Fe(II)_2$-OH absorption would be expected at lower wavenumbers (higher wavelengths) than the $Fe(III)_2$-OH absorptions (Gates 2005), but no such feature is observed in the ATR spectra of the Fe(II)-bearing samples, likely due to stronger overlapping H_2O features.

The tetrahedral Si-O stretching and bending modes occur between 400 and 1200 cm^{-1} (Fig. 6b). In all of the ferruginous smectite samples, the Si-O stretching mode in the tetrahedral sheet occurs around 985 cm^{-1}, and the Si-O-Si bending mode occurs between 415–440 cm^{-1} in the Fe(III) bearing samples and 430–460 cm^{-1} in the Fe(II) bearing samples. The stretching mode does not demonstrate a significant dependence on composition, but the bending mode moves to longer wavenumbers as Fe content increases in all samples. A band near 485 cm^{-1} attributed to the $Fe(III)_{oct}$-O-Si_{tet} bending mode is apparent in samples with at least 30% Fe(III); the shoulder shifts to 510 cm^{-1} in samples C, D, G, and I with an increase in Al in the octahedral sheet, implying the presence of an Al-O-Si bending mode (Madejová and Pálková 2017). The feature around 515 cm^{-1} in the more aluminous Fe(II)-bearing samples M, N, and P is also ascribed to the same Al-O-Si bending mode.

The fundamental octahedral cation-OH bending modes also occur in the same region as the Si-O fundamental absorptions. An asymmetric band at 680 cm^{-1}, present in all of the Fe(III)-bearing samples, is attributed to interactions between the bending of the Fe-O out-of-plane bend and Si-O vibrations, and in more tri-octahedral samples H and J overlaps the Mg_2-OH bend at 656 cm^{-1} (Grauby et al. 1994; Frost and Kloprogge 2000b; Gates 2005). The Fe(II)-bearing samples have less well-defined features in this region than the Fe(III)-bearing samples, but have a very broad plateau between 658–570 cm^{-1} caused by overlapping Mg_2-OH, Fe(II)-Fe(III)-OH, and $Fe(II)_2$-OH bending modes that are not well distinguished. The Fe(III)-bearing samples also exhibit a pair of bands at 815–817 and 870 cm^{-1} that are attributed to the $Fe(III)_2$-OH and the Fe(III)-Al-OH bends (Grauby et al. 1994; Gates 2005; Andrieux and Petit 2010). The 817 cm^{-1} band is only apparent in samples A–E and disappears with decreasing Fe. The Fe-Al-OH bend is also detectable in the Fe(II)-bearing samples, although it has reduced spectral contrast.

Diffuse infrared reflectance. Similar to reflectance spectra in the visible and near-infrared, mid-infrared reflectance spectra depend on both the real and imaginary component of the complex index of refraction. However, while the real component is relatively constant from the visible out to about 5–6 μm such that spectra in the visible to near infrared are practically a function of only the variation in the imaginary component, both the real and imaginary components vary significantly through the infrared region, causing both reflectance minima and maxima that are telling of the mineralogy. Spectral features between ~4000 and 100 cm^{-1} (2.5–25 μm) are caused by the fundamental bending and stretching modes of hydroxyl bonds in the octahedral sheets and silicate structures in the tetrahedral sheets, as well as molecular water within the structure (Fig. 7).

As in the ATR spectra, the presence of interlayer and adsorbed H_2O causes the deep, broad absorptions centered at 2.94 μm (3400 cm^{-1}) and 3.12 μm (3200 cm^{-1}) (Clark et al. 1990; Bishop et al. 1994). The depth of this feature depends on the abundance of water molecules within the interlayer. Superimposed on the fundamental H_2O stretches are the narrower stretching modes of the cations bound to the hydroxyl molecules within the octahedral sheets (Fig. 7a). In the Fe(III) samples, absorption minima shift from ~2.79 to 2.75 μm with decreasing Fe(III) content (Fig. 7b). All samples except for H and J have the deepest metal-OH stretching minimum between 2.80–2.82 μm (3560–3540 cm^{-1}),

consistent with Fe(III) being the controlling cation in the octahedral sheets. The $Fe(III)_2$-OH stretch occurs at 2.80 µm (3560 cm^{-1}) (Madejová et al. 1994) and is most prominent in samples A and B. Samples C, D, E, and F have band minima shifted approximately linearly toward 2.75 µm (3635 cm^{-1}) due to the presence of aluminum and the Al_2-OH stretching mode. Samples H and J, having the least Fe(III) within the octahedral sheets, show distinct, narrow minima at 2.721 µm (3674 cm^{-1}), which are attributed to the Mg-OH-Mg stretching modes. As with the Fe(III)-bearing samples, the minima of the Fe(II)-bearing samples also shift linearly to longer wavelengths and shorter wavenumbers with increasing Fe(II) from 2.72–2.76 µm (3680–3624 cm^{-1}) (Fig. 7b).

The mid-infrared region between 100 and 1200 cm^{-1} contains information about both the octahedral and tetrahedral sheets, as both the fundamental bending modes of the octahedral cation-OH bonds and the bending and stretching modes of the Si-O bonds in the tetrahedral sheet occur in this range (Fig. 8). Features are similar to those observed in the ATR spectra, although the band positions are shifted, and as the reflectance is sensitive to both the absorption and scattering coefficients, display features related to changes in both the real and imaginary component of the index of refraction. All samples have a strong peak centered between 1030–1045 cm^{-1} that is attributed to the fundamental Si-O stretch. The position of this feature does not demonstrate a clear trend as a function of composition in the Fe(III)-bearing samples but does shift to larger wavenumbers in the more aluminous Fe(II)-bearing samples (Fig. 8d). A peak around 455 cm^{-1}, which ranges from 410 to 480 cm^{-1} with decreasing Fe, is attributed to the Si-O bending mode (Frost and Kloprogge 2000b) (Fig. 8b). The dioctahedral samples A, B, C, D, E, F, and G all have secondary peaks between 490–510 cm^{-1}; samples A and B, in particular, have the most distinct secondary peaks centered at 500 cm^{-1}, attributed to the $Fe(III)_{tet}$-O-Si bending modes, due to Fe substitution into the tetrahedral sheet (Frost and Kloprogge 2000b; Madejová and Pálková 2017). The secondary peaks in the other dioctahedral samples are weaker relative to the tetrahedral Fe(III) as they are caused by out-of-plane Fe-O bend, between the tetrahedral and octahedral sheets. The trioctahedrally coordinated samples, particularly H and J, typically show only a single Si-O bending peak but have a pronounced shoulder near 530 cm^{-1} attributed to the Mg-O out-of-plane bending mode (Gates et al. 2017). Samples N and O in the Fe(II)-bearing samples appear double peaked in this spectral region, consistent with the peak splitting of the (06,33) peak in the XRD indicating multiple clay domains, i.e., a partial trioctahedral and dioctahedral nature.

The fundamental bending modes of the octahedral cation-OH bonds occur between 600 and 1000 cm^{-1}. All of the Fe(III)-bearing samples have a broadband near 845 cm^{-1} that does not manifest in the Fe(II)-bearing samples. This bending feature is assigned to $Fe(III)_2$-OH in the dioctahedral samples and Fe-Mg-OH in the trioctahedral Fe(III)-bearing samples (Keeling et al. 2000; Gates 2005). The peak center shifts to shorter wavenumbers as the Mg content of the samples increase, and the Fe content decreases (Fig. 8c). Samples A–D also have a shallow, broad peak near 906 cm^{-1}, which is attributed to the Al-OH-Fe(III) bending mode (Andrieux and Petit 2010).

Samples A–G have a low-intensity, very broad plateau between 745–802 cm^{-1} caused by overlapping contributions of OH bending modes and tetrahedral Si vibrations (Gates 2005). The shoulders are better resolved as a function of increasing Fe content; the bands associated with the feature are the Fe-Al-OH and Fe-Mg-OH bends, which are broadened by lattice deformations caused by irregular cation substitution (Grauby et al. 1994; Gates 2005; Andrieux and Petit 2010).

All samples save O and N exhibit a weak Fe-O out-of-plane bending mode between octahedral Fe and Al and the bridging oxygen that contributes to an asymmetrical, broad peak around 687 cm^{-1} (Grauby et al. 1994; Gates 2005). This feature overlaps

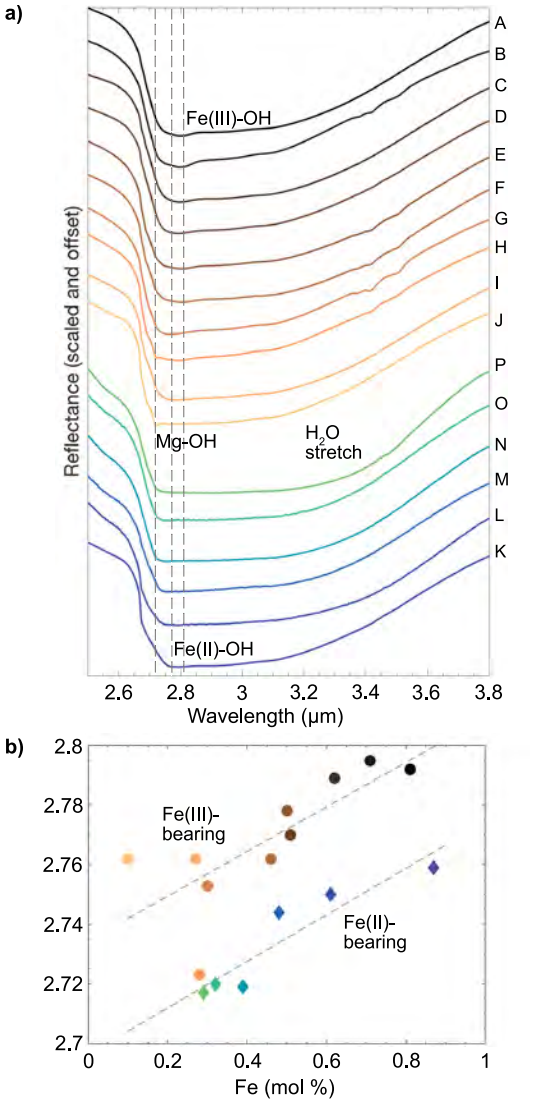

Figure 7. (**a**) Mid-infrared Diffuse Reflectance spectra of the M-OH stretching modes of the sample suite. The deep broad feature around 3 µm is caused by the fundamental H_2O stretching mode, and the narrower absorptions superimposed are the M-OH absorptions. (**b**) The position of the M-OH absorption as a function of octahedral iron content. The minima of both sample sets shifts to longer wavelengths with increasing octahedral iron, but the Fe(II)- and Fe(III)-bearing samples are offset from each other.

with the Mg-Mg-OH bend that occurs closer to 630 cm^{-1}, which is most apparent in samples H and J.

Raman spectroscopy

Raman spectroscopy probes the vibrational modes within the mineral structure, similar to IR spectroscopy methods, but not all bond structures are active in both the IR and Raman, so the two methods are frequently complementary. Like IR measurements, Raman spectroscopy is useful for identifying the stretching and bending modes of the octahedral M-OH interactions and the tetrahedral silicate structure. Smectite clays do not generally have strong Raman responses, due to the low crystallinity and small grain sizes that characterize clay minerals. In particular, the Fe(II)-bearing samples in this study have lower measured intensities and greater photoluminescence effects that obscure features relative to the Fe(III)-bearing samples.

532 nm green Raman. The Raman spectra produced using the 532 nm excitation laser are shown in Figure 9. Most of the Raman peaks between 100 and 1100 cm^{-1} contain information about the tetrahedral bonds (Fig. 9b). All of the samples have a peak near 185 cm^{-1}. It is sharply defined in the Fe(III)-bearing samples and sample P and is detectable but weaker in samples with increasing Fe(II) content. There is not a significant positional change as a function of composition (Fig. 9d). Similar peaks near 187 cm^{-1} observed in other nontronites were ascribed to an octahedral asymmetric $Fe(III)_{oct}$-O_{tet} stretching vibration (Frost and Kloprogge 2000a).

A pair of bands at 245 and 280 cm^{-1} occur in all of the Fe(III)-bearing samples (Fig. 9b). In Fe(III)-rich samples, both peaks are evident, and the 245 cm^{-1} peak is better resolved, whereas in the trioctahedral sample J only the 280 cm^{-1} peak is detected. The intensity and FWHM of the 245 cm^{-1} peak decreases as Mg content increases. In the Fe(II)-bearing samples, peaks around 255 cm^{-1} are poorly resolved in samples O and M, but the signal intensity in all of the Fe(II)-bearing clays make identification challenging. These features are attributed to a lattice deformation between the non-bridging oxygen atoms within the tetrahedral structure and the octahedral OH molecules (Frost and Kloprogge 2000a).

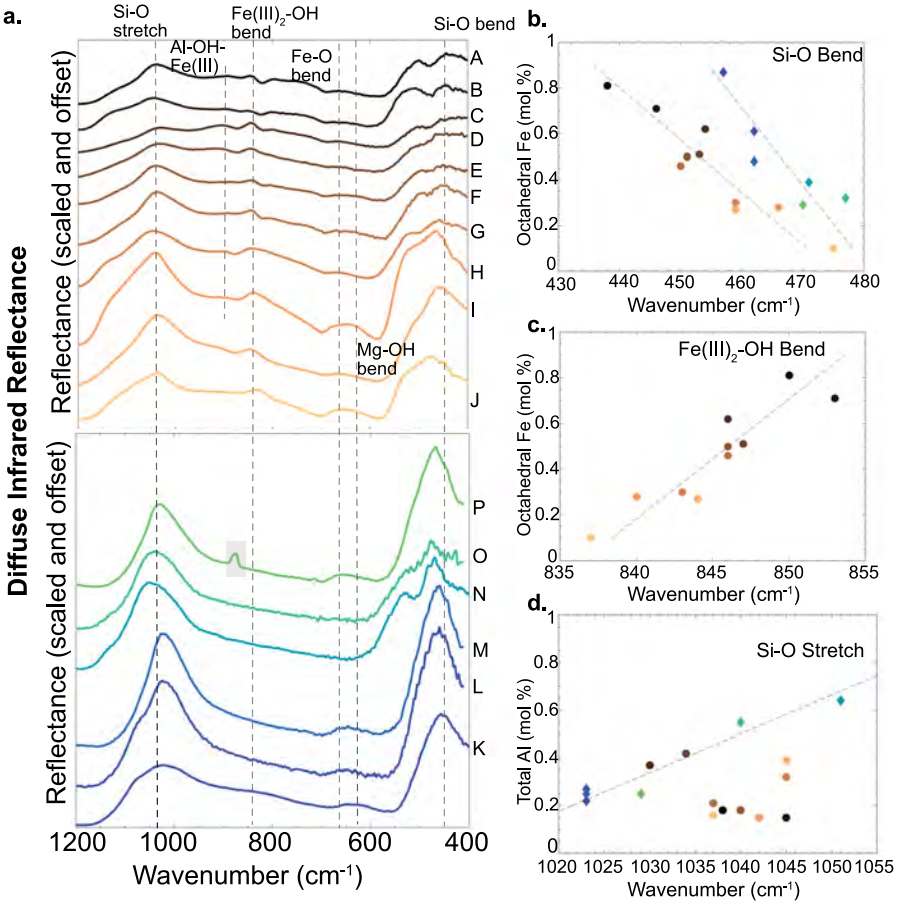

Figure 8. (**a**) Mid-infrared Diffuse Reflectance spectra of the silicate bending and stretching and M-OH bending modes, scaled and offset to emphasize features. A peak attributed to calcite contamination in sample P is indicated by the translucent box. Other peak attributions are discussed in the text. (**b**) The position of the Si-O bend between 430–480 cm^{-1} depends on octahedral Fe content, with decreasing iron shifting the peak position to longer wavenumbers. Fe(II)-bearing samples are offset to longer wavenumbers than Fe(III)-bearing samples. (**c**)The Fe(III) samples show a $Fe(III)_2$-OH bending mode around 845 cm^{-1} that shifts in position as a function of octahedral iron. M-OH bending modes are much more subdued in the Fe(II) samples, although the Fe-OH and Mg-OH bends around 650 cm^{-1} are apparent in all samples. (**d**) The position of the Si-O stretch does not shift as a function of composition in the Fe(III)-bearing samples, but increasing Al content in the Fe(II)-bearing samples does shift this mode to larger wavenumbers. The trend line is only fit to the Fe(II) samples.

Peaks observed in the Fe(III) samples at 360, 465, and 676–687 cm^{-1} (Fig. 9b) are all associated with vibrational modes of the SiO_4 unit (Frost and Kloprogge 2000a). The peak at 465 cm^{-1} can be resolved in all samples, although it is much weaker in the Fe(II)-bearing samples due overlapping features at higher Raman shift, and does not show a compositional dependence. The 465 cm^{-1} feature is attributed to the Si-O bending mode in the tetrahedral sheets. The ~680 cm^{-1} feature in shifts in position from longer to shorter wavenumbers as a function of decreasing Fe(III) content, and occurs only as a weak shoulder in the Fe(II)-bearing samples except in sample P where it is well resolved. The 680 cm^{-1} is attributed to Fe(III)-Si-O bending modes between the octahedral and tetrahedral sheets.

Samples J and H have a sharply defined peak at 432 cm^{-1} that is much weaker in the rest of the Fe(III)-bearing samples and is not well resolved in the Fe(II)-bearing samples (Fig. 9b). It is plausible that this is a Mg-related feature, i.e., Mg-O or Mg-OH, given that these two samples tend to exhibit Mg-related features in the IR that are not observed in the other more Fe-rich samples. There is also a broad absorption near 510 cm^{-1} that is detected in all of the Fe(III)-bearing samples except J and is best defined in the aluminous-Fe(III)-bearing samples. Its presence cannot be confirmed in the Fe(II)-bearing samples due to a very broad peak around 600 cm^{-1}, which is the strongest feature in these samples. Weaker peaks around 600 cm^{-1} are also detected in most of the Fe(III)-bearing samples. The peak position of the 600 cm^{-1} peak shifts to shorter wavenumbers with increasing Fe content, although the trend is weak, and there is not a systematic variation in the 510 cm^{-1} band position as a function of composition. Due to the compositional dependencies, both of these features may be related to Fe and Al within the crystal structure (Bishop and Murad 2004; Wang et al. 2015).

The octahedral bonds in phyllosilicates are weaker Raman scatters than the tetrahedral silicate structures (Wang et al. 2015). Between 800–1000 cm^{-1}, there is very low signal-to-noise and very broad features that are tentatively attributed to M-OH bending modes (Bishop and Murad 2004) (Fig. 9b). In samples A–F, there is a shoulder feature near 885 cm^{-1}, and in samples D, E, and F the hump center shifts toward 920 cm^{-1}. Samples K–O also have very weak, broad features centered near 920 cm^{-1}. These features may be consistent with the Al-Fe(III)-OH and Al-Al-OH bending modes, respectively (Bishop and Murad 2004). The signal to noise is insufficient to positively identify other features, as laser interference patterns, particularly apparent in J and H, are on a similar intensity scale (Fig. 9b).

The metal-OH stretching modes show a distinct compositional trend and occur between Raman shifts of 3500–3700 cm^{-1} as broad envelopes of overlapping peaks (Fig. 9c). Broader peaks caused by the Al-FeOH and Fe-FeOH stretches occur at 3630 and 3570 cm^{-1}, respectively, and are detected to varying degrees in all samples except sample J. Sample P is the only Fe(II)-bearing samples with detectable stretching modes due to significant photoluminescence that dominated much of the spectral range in the rest of the samples. Sample P has an overall shape consistent with the Mg-rich samples H and J with the Mg-OH related shoulder at 3685 cm^{-1}, although the spectral contrast is reduced compared to the Fe(III)-bearing samples. A low, broad hump centered at 3400 cm^{-1} in most of the samples is attributed to an H_2O stretching mode, consistent with a hydrated interlayer, and is particularly apparent in samples H, I, J, and K (de Ligny et al. 2013).

248 nm Deep UV Raman. The DUV Raman spectra of the synthetic smectites (Fig. 10a) begin at 800 cm^{-1} due to the use of an edge filter to suppress a second laser emission line at 700 cm^{-1} (252.9 nm). Therefore, any lattice modes of tetrahedral SiO_4 unit or octahedral M-OH bending modes

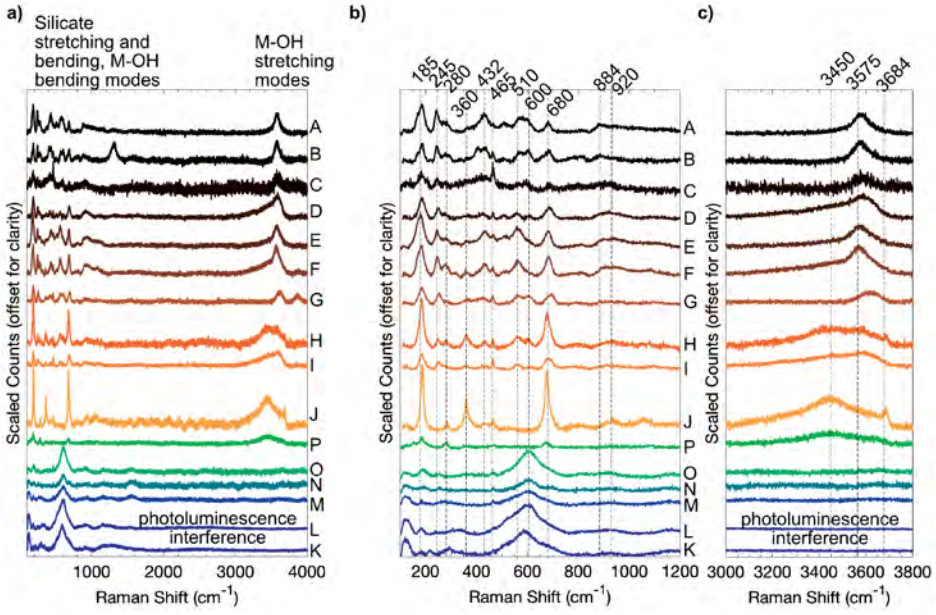

Figure 9. (**a**) Raman patterns obtained using a 532 nm excitation laser. (**b**) Raman shifts between 100–1200 cm^{-1} highlight silicate stretching and bending modes and overlapping metal-OH bends. (**c**) Metal-OH stretching modes occur between 3000–4000 cm^{-1}. Labeled features are discussed in the text.

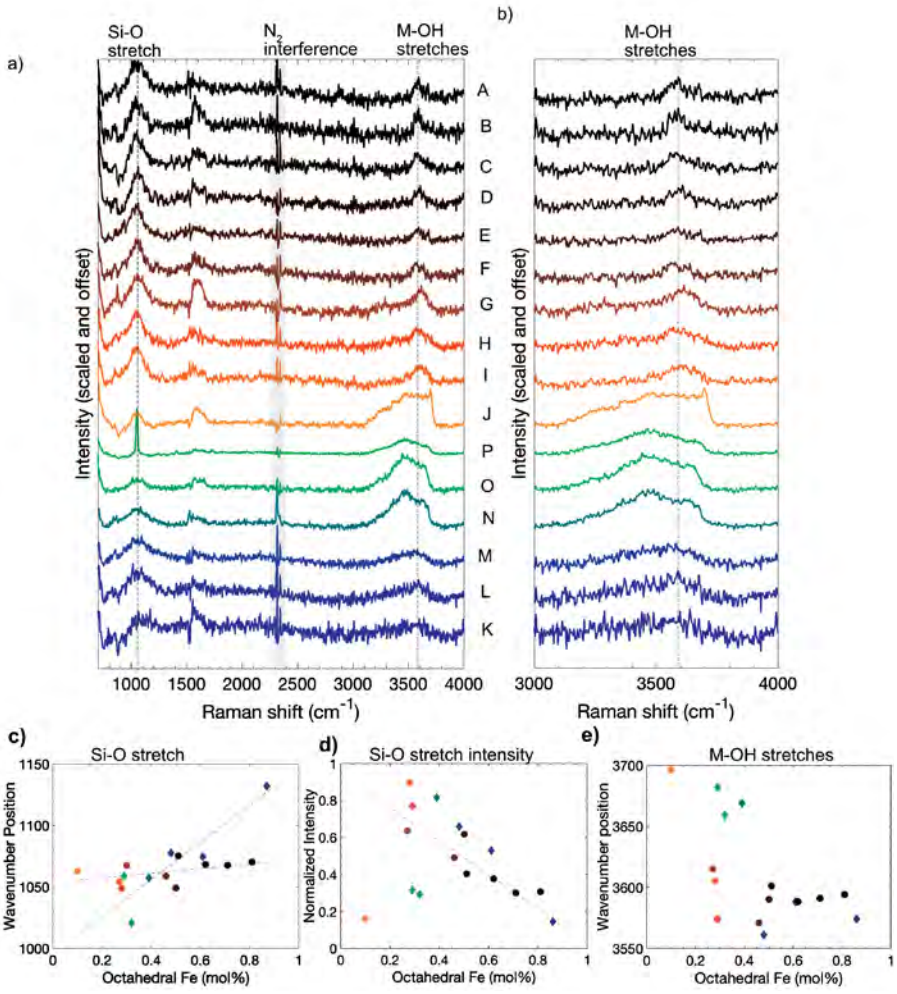

Figure 10. (**a**) Raman spectra obtained using a 248.6 nm excitation laser from 700–4000 cm^{-1}, and (**b**) the M-OH stretching region from 3000–4000 cm^{-1}. (**c**) The Si-O stretching mode is detected around 1060 cm^{-1} and (**d**) the normalized signal intensity decreases as Fe content increases, due to increased UV absorption. (**e**) The peak and shoulder positions of the Fe(II), Fe(III), Al, and Mg-OH stretching modes shift as a function of composition.

between 100–800 cm^{-1} are not recorded. Every sample has a broad (FWHM of 120–300 cm^{-1}) peak feature at approximately 1065 cm^{-1}, attributed to a Si-O stretching mode (Fig. 10c). This peak varies between about 1055 and 1070 cm^{-1}; although the Fe(III)-bearing samples do not demonstrate a clear compositional trend, the Fe(II)-bearing samples show a shift to longer wavelengths with increasing octahedral iron content. The presence of Fe in the samples also had a marked impact on the measured Raman intensity of this Si-O stretch; a clear trend is seen in the integrated peak intensity (after normalization to an internal standard, the atmospheric N_2 signal), which decreased with increasing Fe content (Fig. 10d). This is not unexpected, as smectites are known to have UV absorption bands that are highly dependent on the concentration of octahedral Fe, particularly at ~250 nm, very close to the laser excitation wavelength (Chen et al. 1979). However, both samples J and O show less intensity than the trend would predict for Fe-poor smectite. The intensity of sample P is also compromised by a strong Raman reflectance peak near 1075 cm^{-1} caused by minor calcite contamination that formed after synthesis.

The Metal-OH stretching modes show demonstrable compositional trends (Figs. 10b and 10e), and unlike in the Green Raman spectra, the Fe(II)-bearing smectite spectra are not photoluminescence dominated, such that stretching modes can be detected. Samples J, P, O, and N have a broad, multi-modal peak between 3300 and 3700 cm^{-1} consistent with the stretching mode of interlayer H_2O. These samples also have distinct shoulders or superimposed peaks around 3660 and 3700 cm^{-1}, which, although shifted, are attributed to Mg and Al-OH stretching modes. Fe(III)-bearing samples A–I, and Fe(II)-bearing samples K, L, and M all have low-intensity peaks that vary between 3560 and 3620 cm^{-1} with no systematic dependence on Fe or Al content. This feature is attributed to Fe-OH stretching, although there is not a clear distinction between Fe(III) and Fe(II) bonds.

A minor peak is observed at ~1600 cm^{-1} in all samples, although the intensity relative to the 1050 cm^{-1} peak varies widely

and shows non-systematic compositional trends (Fig. 10a). This peak is not easily assigned, as few studies for which Raman spectra are reported for smectites and other clay minerals have considered the 1400–3000 cm^{-1} region (Frost and Kloprogge 2000; Wang et al. 2015). The peak occurs in the same frequency range as either an H_2O bending mode or the C=C stretching mode (Ferrari and Robertson 2001; Bishop and Murad 2004; Socrates 2004), e.g., the "G" band of carbonaceous material (Schopf et al. 2005; Quirico et al. 2009). As the H_2O content does not show large variation in the IR or Green Raman measurements, we tentatively assign the strongest ~1600 cm^{-1} peaks to a possible organic contaminant, which may have been picked up during handling. Although a corresponding peak is not definitively observed under 532 nm excitation in samples other than P, N, and M, selective detection of carbon-rich contaminants using 248 nm excitation can be attributed to a resonant enhancement of C=C vibrations associated with π-π* absorption in the UV (Asher and Johnson 1984; Beegle et al. 2015; Sapers et al. 2019). Previous studies using the same UV Raman instrument have shown that the resonant Raman scattering from certain carbon-rich compounds, such as polycyclic aromatics, can be detected at concentrations as low as 0.1 ppm within mineral matrices (Abbey et al. 2017).

Mössbauer spectroscopy

The significant difference in isomer shift between ferrous and ferric iron makes Mössbauer spectroscopy a useful technique to determine iron oxidation state. In general, a Mössbauer spectrum will display a quadrupole doublet for each type of coordination environment. The center of the two lines, the isomer shift, depends on various factors of which oxidation state and coordination geometry are most important in clays. In addition to the isomer shift, information about the electric field gradient can be gleaned from the quadrupole splitting (ΔE_Q), which can be used to distinguish different coordination environments.

Mössbauer data were collected on 11 out of 16 species (Fig. 11). Data collection of samples G–J and P was hampered by the low concentrations of iron, especially because samples were not synthesized using ^{57}Fe-doped material. The Mössbauer spectra collected for samples A–F show either an unresolved quadrupole doublet or quadrupole doublets with a small quadrupole splitting (Fig. 11a). The small quadrupole splitting for these samples is characteristic of high-spin Fe(III) in an octahedral coordination environment. Although the spectra of A–F are broad, they can be fit well with a single quadrupole doublet with isomer shifts between 0.34 and 0.36 mm s^{-1} (Table 5). These isomer shifts are characteristic of octahedral Fe(III) sites (Burns 1993) and within the range of Fe(III) smectites (0.33–0.37 mm s^{-1}) (Murad and Schwertmann 1984; Treiman et al. 2014). No ferrous material is present based on the absence of quadrupole doublets with an isomer shift above 1.0 mm s^{-1} (Chemtob et al. 2015). For sample A, an improved fit was obtained with a small tetrahedral site Fe component (7.5%), resulting in an isomer shift of 0.25 and quadrupole splitting of 1.50, but the large overlap between peaks also produced high uncertainty.

The Mössbauer spectra collected for K-O show a quadrupole doublet centered between 1.10 and 1.15 mm s^{-1} characteristic for octahedral Fe(II) and a smaller broad unresolved quadrupole doublet due to Fe(III) (Fig. 10b; Table 5). Most spectra of K-O can be fit with well with a single quadrupole doublet with linewidths between 0.4–0.5 mm s^{-1}. The high isomer shifts observed (>1 mm s^{-1}) are characteristic of octahedral Fe(II) sites and are comparable to those observed for similar Fe(II) smectites (Chemtob et al. 2015). Although the spectra recorded by our other techniques show distinct differences upon changing the iron ratio, the quadrupole splitting and isomer shifts (Table 5; Figs. 10c and 10d) do not show any consistent variation with increasing or decreasing Fe content. The absence of any systematic variation with Fe content is consistent with Mössbauer observations made for the jarosite family (McCollom et al. 2014) and for Fe(II) smectites by Chemtob et al. (2015).

Fitting the areas of the doublets yields Fe(II)/Fe(III) ratios in close agreement with those determined by other techniques (Table 5). The ratios of samples K and L deviate more, which is likely due to oxidation during storage or the handling process of these samples. The Fe(II) ratio measured in sample K decreased between subsequent measurements before and after the sample was handled in air (Online Material[1] Fig. OM1). Due to the oxidation, the ratios only represent a lower bound on the Fe(II) content at the time of synthesis.

As Mössbauer spectra of Fe phases typically have temperature-dependent effects and the temperature of sample measurement can vary under planetary conditions, we investigated the temperature dependency on the isomer shift two samples, Fe(III)-bearing sample A and Fe(II)-bearing K. Spectra were recorded between 80 and 320 K (Fig. 12). In line with work on octahedral Fe(III) by, e.g., DeGraven and Alboom (1991), the isomer shift of both samples exhibits a dramatic decrease of 0.14 mm s^{-1} upon cooling the samples from 320 to 80 K (Table 6). The difference of 0.1 mm s^{-1} between 293 and 80 K is the same that observed for certain nontronites (Murad et al. 1987). No additional hyperfine features were resolved at lower temperatures and therefore the other samples were collected at room temperature, which is also consistent with previous studies (Chemtob et al. 2015; McCollom et al. 2014; Morris et al. 2006).

Implications for planetary remote sensing and in situ exploration

This study demonstrates the synergies and limits of multiple measurement types for the detection of smectite chemistry and oxidation state on planetary surfaces to infer past geochemical conditions. Reflectance spectroscopy has previously been shown to detect alteration minerals, including smectite clays, at levels ~10% in natural mineral assemblages (Ehlmann et al. 2012; Greenberger et al. 2012). We demonstrate that smectite composition and the dominant oxidation state of Fe in the octahedral state can be identified in the near infrared on the basis of their metal-OH vibrational modes. The 2.0–3 μm region is particularly useful. The fundamental M-OH stretching modes between 2.6–2.9 μm vary systematically with chemistry, and the metal-OH minimum wavelength increases for smectites with Mg, Al, Fe(II), and Fe(III), respectively. Smectites dominated by Mg or Fe(III) are spectrally distinct, whereas Al-rich and Fe(II)-rich smectites both have minima near 2.76 (Fig. 7). This absorption has been interpreted to represent Al phyllosilicates in Ceres bright spots (De Sanctis et al. 2015), but our study shows that the spectral pattern would also be consistent with the presence

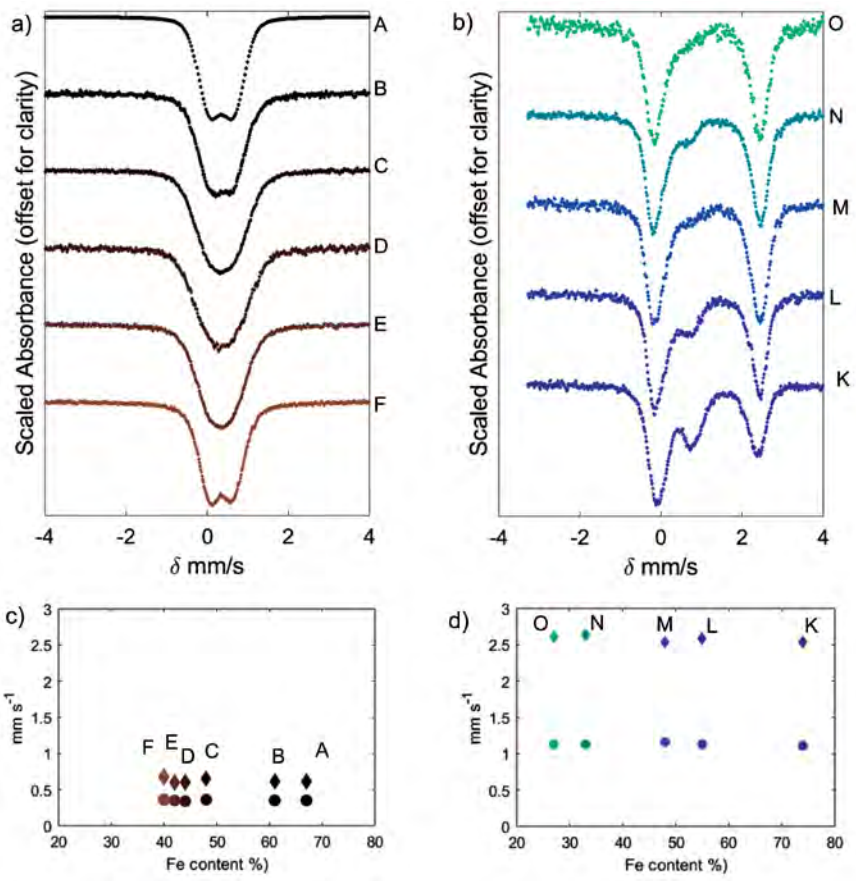

Figure 11. Mössbauer spectra for (**a**) Fe(II)-bearing smectite samples A–F at room temperature and (**b**) of Fe(II)-bearing smectite samples K-O. The isomer shifts are shown as diamonds and the quadrupole splitting ΔE_Q is shown as circles for the (**c**) Fe(II)-bearing samples and (**d**) Fe(II)-bearing samples.

Table 5. Isomer shift and quadrupole splitting of the Fe-rich smectite samples

Smectite	Fe^{II} δ (mm s^{-1})	Fe^{II} ΔE_Q (mm s^{-1})	Fe^{III} δ (mm s^{-1})	Fe^{III} ΔE_Q (mm s^{-1})	Fe^{II}/Fe^{III}
A	–	–	0.35 ± 0.02	0.61 ± 0.01	0
B	–	–	0.35 ± 0.02	0.61 ± 0.01	0
C	–	–	0.36 ± 0.02	0.64 ± 0.01	0
D	–	–	0.36 ± 0.02	0.67 ± 0.01	0
E	–	–	0.34 ± 0.02	0.59 ± 0.01	0
F	–	–	0.35 ± 0.02	0.60 ± 0.01	0
K	1.11 ± 0.02	2.53 ± 0.01	0.40 ± 0 .02	0.77 ± 0.01	77.2
L	1.13 ± 0.02	2.59 ± 0.01	0.42 ± 0.02	0.61 ± 0.01	72.1
M	1.16 ± 0.02	2.54 ± 0.01	0.44 ± 0.02	0.58 ± 0.01	91.8
N	1.13 ± 0.02	2.63 ± 0.01	0.40 ± 0.02	0.55 ± 0.01	85.1
O	1.13 ± 0.02	2.61 ± 0.01	0.39 ± 0.02	0.55 ± 0.01	88.8

of Fe(II) smectites. Use of multiple wavelength regions in the NIR can yield unique solutions, if overtone and combination absorptions are present in remotely sensed data. The ~2.24 μm absorption tracks Mg substitution well, and the M-OH feature near 2.32 is diagnostic of Fe(III) vs. Fe(II), shifting considerably with Mg substitution in Fe(II) smectites only (Fig. 5). This multiple wavelength approach extends previous analyses of the 2.3 μm's variation with octahedral sheet occupancy and iron content (Michalski et al. 2015). The overtone and fundamental H_2O stretches at 1.9 and 3 μm provide additional information on the degree of hydration in smectites. The visible wavelength region can provide qualitative auxiliary information about Fe oxidation, but the electronic absorptions observed between 0.4–1 μm are not unique to smectite clays, so the M-OH features are more diagnostic of smectite speciation, particularly in mineral assemblages.

As instrument builders consider implementation approaches, spatial and spectral resolution, as well as signal-to-noise (SNR), are key considerations to enable discrimination of the diagnostic absorptions. Many NIR reflectance spectrometers, such as the Mars Express/OMEGA, MRO/CRISM, Dawn/VIR, Osiris-Rex/OVIRS, and Cassini/VIMS, are sensitive from ~1–4/5 μm with sufficient spectral resolution to distinguish the features discussed above and provide global views of planetary surfaces at relatively large pixel footprints between tens and hundreds of meters square. Higher spatial resolution, of course, allows mineral identifications to be better associated with particular strata or geomorphic features, improving geologic interpretations and providing further constraints on alteration environments. Detailed analysis of spectral variation on the hand-sample scale (millimeters-centimeters) is particularly useful to identify alteration textures and spatial patterns, all of which provide key context in understanding the alteration environment. Such fine resolution VNIR spectral analysis will be employed for the first time on Mars onboard the Mars 2020 rover by the SuperCam instrument (Wiens et al. 2017) and on the Exo-Mars rover by Ma_MISS (De Sanctis et al. 2017) and micrOmega (Bibring et al. 2017).

In the mid-infrared, the silicate stretching and bending modes active in smectite clays are common to other silicates as well, and the M-OH bending modes are discernable but overlap and combine, making direct identification of a particular smectite

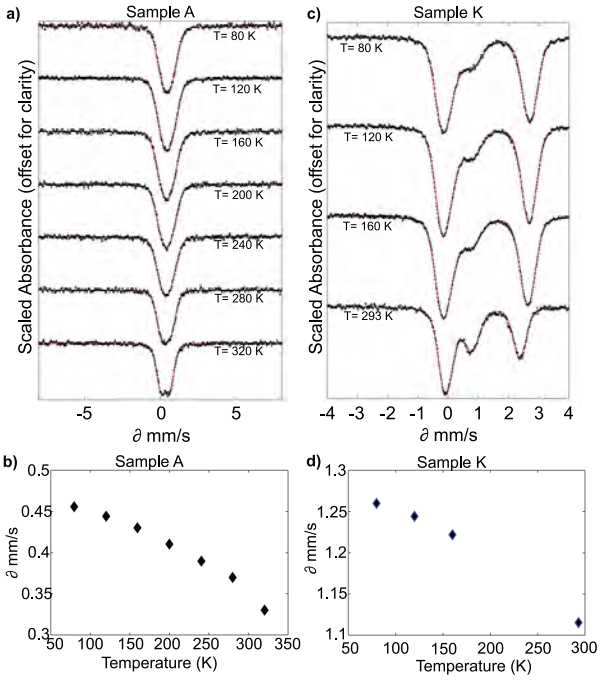

Figure 12. The Isomer shift is temperature dependent. (**a**) Mössbauer spectra of sample A collected from 80 to 320 K with 40 K intervals in black and the fit in red. The spectra are referenced to the centroid of the spectrum of a α-Fe foil at room temperature. (**b**) The isomer shift of A decreases as a function of increasing temperature. (**c**) Mössbauer spectra of sample K collected from 80 to 293 K. (**d**). The isomer shift of K decreases as temperature increases.

species challenging, particularly if the measurement is of a bulk mineral assemblage. Michalski et al. (2005) demonstrated how the Si-O and M-O bends changed in character between dioctahedral and trioctahedral smectites. Here we demonstrate that the 450 cm^{-1} absorption systematically varies in position with octahedral Fe(III) and Fe(II) content, although other information from the VNIR (or Mössbauer in situ) must be brought to bear to determine the oxidation state and the micromega relationship between absorption position and Fe content (Fig. 8b). The Mars Global Surveyor Thermal Emission Spectrometer (TES) and Mars Exploration Rover Mini-TES thermal emission instruments in orbit around and on the surface of Mars, respectively, have been used with this multi-instrument approach to conduct surveys with other orbiting or payload elements specifically characterizing smectite minerals and alteration phases (Michalski et al. 2006, 2010; Ruff and Christensen 2007). OTES on Osiris-REX, along with OVIRS, is also characterizing the phyllosilicates on the asteroid Bennu (Hamilton et al. 2019). With our expanded spectral libraries, more refined characterization of smectites from MIR data is now possible.

Raman spectroscopy is a new addition to planetary science instrumentation and is opening new avenues for in situ remote mineralogical analysis of planetary surfaces, as well as the detection of organic components. The green Raman SuperCam Raman system is designed to obtain patterns from several meters distant to the target from on the mast of the Mars 2020 rover (Wiens et al. 2017), and the deep-UV Raman SHERLOC system will interrogate rock surfaces on the micrometer scale from its position on the Mars 2020 rover arm (Beegle et al. 2017). Our data provide the first Raman spectral libraries as a function of their chemistry (Figs. 9 and 10). Precise identification of smectite clays, and clay minerals in general, will likely be a challenge in natural mineral assemblages due to the generally low Raman intensities inherent to clay minerals and sensitivity to complex lattice variation. However, the M-OH stretching modes between 3000–4000 cm^{-1} in both Green and Deep UV Raman data sets will be useful for identifying phyllosilicates and qualitatively judging their composition. In both Raman excitation modes, it is possible in some cases to detect the Fe(III), Al, and Mg-OH stretching modes, although intensity decreases significantly as Fe content increases. The M-OH bending modes and silicate features between 400–1000 cm^{-1} require high signal-to-noise to be distinguished and are likely to be overlapping with more crystalline phases in natural mineral assemblages that would mask phyllosilicate detection. Photoluminescence, which is frequently much stronger than Raman signal, is also a likely obstacle in identifying mineral assemblages on planetary surfaces; Fe(II)-bearing smectites are apparently more susceptible to photoluminescence when using a 532 nm excitation laser than DUV (Fig. 10). Carrying more than one excitation laser, as the Mars 2020 rover is planning, may help mitigate photoluminescence concerns, as switching wavelengths can reduce the effect for a given material. Thus, Raman is best used in concert with other approaches for characterization smectite-bearing mineral assemblages.

In situ XRD analyses offer the most quantitative means to measure the absolute abundance of smectite clays and their coordination (Fig. 3). The Chemistry and Mineralogy Analyzer instrument (CheMin), an X-ray diffractometer onboard the Mars Science Laboratory Rover Curiosity, has demonstrated the common occurrence of smectite clays in the sedimentary deposits within Gale Crater (Vaniman et al. 2013; Bristow et al. 2018). Notably, our sample set of synthetic smectites have peak positions, as corrected for measurements using Co*K*α radiation (Table 2), that cover the full range of observations of martian smectites in Gale crater (Vaniman et al. 2013; Treiman et al. 2014; Bristow et al. 2018). This demonstrates that, potentially, the compositions of the data set presented here is representative of the martian samples, and that all martian observations can be consistent with the presence of a single smectite, and that mixtures of dioctahedral and trioctahedral phases are not required to describe the features observed (e.g., Bristow et al. 2018). The CheMin instrument requires the use of the position of the (02,11) peak to calculate the octahedral site occupancy of smectites measured in Gale Crater, Mars, as the (06,33) peak

Table 6. Variation in the isomer shift in samples A and K as temperature is adjusted

Temperature (K)	δ (mm s^{-1}) – Sample A	δ (mm s^{-1}) – Sample K
80	0.46 ± 0.01	1.26 ± 0.01
120	0.44 ± 0.01	1.24 ± 0.01
160	0.43 ± 0.01	1.22 ± 0.01
200	0.41 ± 0.01	–
240	0.39 ± 0.01	–
280	0.37 ± 0.01	–
293	0.35 ± 0.01	–
310	0.35 ± 0.01	1.15 ± 0.01
320	0.33 ± 0.01	1.13 ± 0.01

occurs outside the diffraction range. Our results demonstrate that it is critical to recognize that peak positions of the (02,11) bands produce substantial systematic errors if used to obtain lattice parameters of smectites. Use of the (06,33) band peak positions, widely employed in terrestrial studies of clays but inaccessible by the ChemMin instrument on MSL, yields an order of magnitude smaller systematic error. Thus, as with prior investigations, our study shows the value of incorporating the (06,33) peak into instrument diffraction ranges to best distinguish dioctahedral and trioctahedral smectites. In most laboratory settings, clay mineral fractions are separated from the rest of the sample, making measurements more straightforward, but martian samples are measured in bulk, which can further obfuscate precise analysis and calculation of lattice parameters. Consequently, identifications of specific phyllosilicate phases are most easily made when applying secondary information. On the Curiosity rover, this is water release temperature from Evolved Gas Analysis with the SAM instrument (Bristow et al. 2015). VNIR, MIR, and Mössbauer are also highly synergistic because they provide information on the Fe oxidation state that XRD alone cannot.

Mössbauer spectra can aid in confirming detections of smectite minerals using the measured isomer shifts and patterns in quadrupole splittings. Particularly, Mössbauer measurements provide a quantitative and highly sensitive means to determine Fe(II)/Fe(III) ratios better than all other analysis techniques discussed here but do not demonstrate uniquely identifying patterns that distinguish smectites of varying quantitative Fe content from one another. Consequently, Mössbauer spectroscopy is best utilized in conjunction with other in situ approaches to examine alteration mineralogy. The Mössbauer parameters reported here, derived from room-temperature measurements, can be used in direct comparison to extra-terrestrial Mössbauer measurements, despite overall ambient-temperature differences between the library and in situ measurements (Morris et al. 2006). The temperature dependence of Mössbauer measurements derives from the temperature gradient between the sample and the source. This gradient highlights hyperfine structures but renders comparisons to measurements made under different conditions ill-posed. However, Mössbauer measurements made in extra-terrestrial settings, such as by the Mars Exploration Rovers, have kept both the source and samples (planetary surfaces) at the same ambient temperature. Our measurements also have a negligible temperature difference between source and sample measured at room temperature, so we thus mitigate the temperature dependencies of the derived parameters, creating a database for application to determination of smectite presence and Fe.

Collectively, the data presented here are foundational for the study of smectite clays across the solar system. The ability to determine the coordination, crystal chemistry, and oxidation state will enable new insights into the geological and environmental evolution of planetary bodies.

Acknowledgments and Funding

Thanks to George Rossman for the use of his ATR and Raman instruments, as well as sage advice. Thanks also to Rohit Bhartia for use of the DUV Raman system. We also thank our reviewers, Benoit Dubacq and Jebril Hadi, for extremely thoughtful reviews that greatly improved the quality of our manuscript. This work was funded by NASA Solar Systems Workings (NNX15AH53G), Mars Science Laboratory Participating Scientist, and Mars 2020 SHERLOC Co-Investigator grants, all to B.L.E.

References cited

Abbey, W.J., Bhartia, R., Beegle, L.W., DeFlores, L., Paez, V., Sijapati, K., Sijapati, S., Williford, K., Tuite, M., Hug, W., and others (2017) Deep UV Raman spectroscopy for planetary exploration: The search for in situ organics. Icarus, 290, 201–214.

Ammannito, E., DeSanctis, M.C., Ciarniello, M., Frigeri, A., Carrozzo, F.G., Combe, J.-P., Ehlmann, B.L., Marchi, S., McSween, H.Y., Raponi, A., and others (2016) Distribution of phyllosilicates on the surface of Ceres. Science, 353, aaf4279.

Andrieux, P., and Petit, S. (2010) Hydrothermal synthesis of dioctahedral smectites: The Al-Fe^{3+} chemical series: Part I: Influence of experimental conditions. Applied Clay Science, 48, 5–17.

April, R.H., and Keller, D.M. (1992) Saponite and vermiculite in amygdales of the Granby Basaltic Tuff, Connecticut Valley. Clays and Clay Minerals, 40, 22–31.

Arvidson, R.E., Squyres, S.W., Bell, J.F., Catalano, J.G., Clark, B.C., Crumpler, L.S., de Souza, P.A., Fairén, A.G., Farrand, W.H., Fox, V.K., and others (2014) Ancient aqueous environments at Endeavour Crater, Mars. Science, 343.

Asher, S.A., and Johnson, C.R. (1984) Raman spectroscopy of a coal liquid shows that fluorescence interference is minimized with ultraviolet excitation. Science, 225, 311–313.

Badaut, D., Besson, G., Decarreau, A., and Rautureau, R. (1985) Occurrence of a ferrous, trioctahedral smectite in recent sediments of Atlantis II Deep, Red Sea. Clay Minerals, 20, 389–404.

Beegle, L., Bhartia, R., White, M., DeFlores, L., Abbey, W., Wu, Y.-H., Cameron, B., Moore, J., Fries, M., Burton, A., and others (2015) SHERLOC: Scanning habitable environments with Raman and luminescence for organics and chemicals. 2015 IEEE Aerospace Conference pp. 1–11. Presented at the 2015 IEEE Aerospace Conference.

Beegle, L.W., Bhartia, R., Carrier, B., DeFlores, L., Abbey, W., Asher, S., Burton, A., Fries, M., Conrad, P., Clegg, S., and others (2017) The SHERLOC Investigation. Lunar and Planetary Science Conference, 2839.

Bergmann, J., Friedel, P., and Kleeberg, R. (1998) BGMN—A new fundamental parameters based Rietveld program for laboratory X-ray sources, its use in quantitative analysis and structure investigations. Commission on Powder Diffraction (IUCr) Newsletter, 20, 5–8.

Besson, G., and Tchoubar, C. (1972) Détermination du groupe de symétrie du feuillet élémentaire de la beidellite. Comptes Rendus Hebdomadaires des Séances de l'Académie Des Sciences Serie D, 275, 633–636.

Bibring, J.-P., Langevin, Y., Mustard, J.F., Poulet, F., Arvidson, R., Gendrin, A., Gondet, B., Mangold, N., Pinet, P., Forget, F., and others (2006) Global Mineralogical and Aqueous Mars History Derived from OMEGA/Mars Express Data. Science, 312, 400–404.

Bibring, J.-P., Hamm, V., Pilorget, C., Vago, J.L., and the MicrOmega Team. (2017) The MicrOmega Investigation Onboard ExoMars. Astrobiology, 17, 621–626.

Bishop, J.L., and Murad, E. (2004) Characterization of minerals and biogeochemical markers on Mars: A Raman and IR spectroscopic study of montmorillonite. Journal of Raman Spectroscopy, 35, 480–486.

Bishop, J.L., Pieters, C.M., and Edwards, J.O. (1994) Infrared spectroscopic analyses on the nature of water in montmorillonite. Clays and Clay Minerals, 42, 702–716.

Bishop, J. L., Dobrea, E.Z.N., McKeown, N.K., Parente, M., Ehlmann, B.L., Michalski, J.R., Milliken, R.E., Poulet, F., Swayze, G.A., Mustard, J.F., and others (2008a) Phyllosilicate diversity and past aqueous activity revealed at Mawrth Vallis, Mars. Science, 321, 830–833.

Bishop, J.L., Lane, M.D., Dyar, M.D., and Brown, A.J. (2008b) Reflectance and emission spectroscopy study of four groups of phyllosilicates: Smectites, kaolinite-serpentines, chlorites and micas. Clay Minerals, 43, 35–54.

Brindley, G.W., and Brown, G. (1980) Crystal structures of clay minerals of clay minerals and their X-ray identification. Mineralogical Society Monograph.

Bristow, T.F., Bish, D.L., Vaniman, D.T., Morris, R.V., Blake, D.F., Grotzinger, J.P., Rampe, E.B., Crisp, J.A., Achilles, C.N., Ming, D.W., and others (2015) The origin and implications of clay minerals from Yellowknife Bay, Gale crater, Mars. American Mineralogist, 100, 824–836.

Bristow, T.F., Rampe, E.B., Achilles, C.N., Blake, D.F., Chipera, S.J., Craig, P., Crisp, J.A., Marais, D.J.D., Downs, R.T., Gellert, R., and others (2018) Clay mineral diversity and abundance in sedimentary rocks of Gale crater, Mars. Science Advances, 4, eaar3330.

Bunch, T.E., and Chang, S. (1980) Carbonaceous chondrites—II. Carbonaceous chondrite phyllosilicates and light element geochemistry as indicators of parent body processes and surface conditions. Geochimica et Cosmochimica Acta, 44, 1543–1577.

Burns, R.G. (1970) Crystal field spectra and evidence of cation ordering in olivine minerals. American Mineralogist, 55, 1608–1632.

——— (1993) Rates and mechanisms of chemical weathering of ferromagnesian silicate minerals on Mars. Geochimica et Cosmochimica Acta, 57, 4555–4574.

Carter, J., Poulet, F., Bibring, J.-P., Mangold, N., and Murchie, S. (2013) Hydrous minerals on Mars as seen by the CRISM and OMEGA imaging spectrometers:

Updated global view. Journal of Geophysical Research: Planets, 118, 831–858.
Castellini, E., Malferrari, D., Bernini, F., Brigatti, M.F., Castro, G.R., Medici, L., Mucci, A., and Borsari, M. (2017) Baseline studies of the Clay Minerals Society source clay montmorillonite STx-1b. Clays and Clay Minerals, 65, 220–233.
Catalano, J.G. (2013) Thermodynamic and mass balance constraints on iron-bearing phyllosilicate formation and alteration pathways on early Mars. Journal of Geophysical Research: Planets, 118, 2124–2136.
Catling, D.C., and Moore, J.M. (2003) The nature of coarse-grained crystalline hematite and its implications for the early environment of Mars. Icarus, 165, 277–300.
Chemtob, S.M., Nickerson, R.D., Morris, R.V., Agresti, D.G., and Catalano, J.G. (2015) Synthesis and structural characterization of ferrous trioctahedral smectites: Implications for clay mineral genesis and detectability on Mars. Journal of Geophysical Research: Planets, 120, 1119–1140.
——— (2017) Oxidative alteration of ferrous smectites and implications for the redox evolution of early Mars. Journal of Geophysical Research: Planets, 2017JE005331.
Chen, Y., Shaked, D., and Banin, A. (1979) The role of structural iron(III) in the UV absorption by smectites. Clay Minerals, 14, 93–102.
Clark, R.N., King, T.V.V., Klejwa, M., Swayze, G.A., and Vergo, N. (1990) High spectral resolution reflectance spectroscopy of minerals. Journal of Geophysical Research: Solid Earth, 95, 12653–12680.
Curtis, C.D. (1976) Unmixed Ca^{2+}-Mg^{2+} saponite at Calton Hill, Derbyshire. Clay Minerals, 11, 85–89.
Daynyak, L.G., Drits, V.A., Kudryavtsev, D.I., Simanovich, I.M., and Slonimskaya, M.V. (1981) Crystal chemical specificity of trioctahedral smectites: Products of secondary alteration of oceanic and continental basalts. Doklady Akademii Nauk SSSR, 259, 1458–1462.
De Grave, E., and Van Alboom, A. (1991) Evaluation of ferrous and ferric Mössbauer fractions. Physics and Chemistry of Minerals, 18, 337–342.
de Ligny, D., Guillaud, E., Gailhanou, H., and Blanc, P. (2013) Raman spectroscopy of adsorbed water in clays: First attempt at band assignment. Procedia Earth and Planetary Science, 7, 203–206.
De Sanctis, M.C., Ammannito, E., Raponi, A., Marchi, S., McCord, T.B., McSween, H.Y., Capaccioni, F., Capria, M.T., Carrozzo, F.G., Ciarniello, M., and others (2015) Ammoniated phyllosilicates with a likely outer Solar System origin on (1) Ceres. Nature, 528, 241–244.
De Sanctis, M.C., Altieri, F., Ammannito, E., Biondi, D., De Angelis, S., Meini, M., Mondello, G., Novi, S., Paolinetti, R., Soldani, M., and others (2017) Ma_MISS on ExoMars: Mineralogical characterization of the martian subsurface. Astrobiology, 17, 612–620.
Decarreau, A., and Bonnin, D. (1986) Synthesis and crystallogenesis at low temperature of Fe(III)-smectites by evolution of coprecipitated gels: Experiments in partially reducing conditions. Clay Minerals, 21, 861–877.
Decarreau, A., Petit, S., Martin, F., Farges, F., Vieillard, P., and Joussein, E. (2008) Hydrothermal synthesis, between 75 and 150 °C, of high-charge, ferric nontronites. Clays and Clay Minerals, 56, 322–337.
Desprairies, A., Tremblay, P., and Laloy, C. (1989) Secondary mineral assemblages in a volcanic sequence drilled during ODP Leg 104 in the Norwegian Sea. Proceedings of the Ocean Drilling Program, Scientific Results, 104, 397–409.
Doebelin, N., and Kleeberg, R. (2015) Profex: a graphical user interface for the Rietveld refinement program BGMN. Journal of Applied Crystallography, 48, 1573–1580.
Ehlmann, B.L., and Edwards, C.S. (2014) Mineralogy of the martian surface. Annual Review of Earth and Planetary Sciences, 42, 291–315.
Ehlmann, B.L., Mustard, J.F., Murchie, S.L., Bibring, J.-P., Meunier, A., Fraeman, A.A., and Langevin, Y. (2011) Subsurface water and clay mineral formation during the early history of Mars. Nature, 479, 53–60.
Ehlmann, B.L., Bish, D.L., Ruff, S.W., and Mustard, J.F. (2012) Mineralogy and chemistry of altered Icelandic basalts: Application to clay mineral detection and understanding aqueous environments on Mars. Journal of Geophysical Research: Planets, 117, E00J16.
Ferrari, A.C., and Robertson, J. (2001) Resonant Raman spectroscopy of disordered, amorphous, and diamondlike carbon. Physical Review B, 64, 075414.
Fox, V.K., Arvidson, R.E., Guinness, E.A., McLennan, S.M., Catalano, J.G., Murchie, S.L., and Powell, K.E. (2016) Smectite deposits in Marathon Valley, Endeavour Crater, Mars, identified using CRISM hyperspectral reflectance data. Geophysical Research Letters, 43, 2016GL069108.
Frost, R.L., and Kloprogge, J.T. (2000a) Raman spectroscopy of nontronites. Applied Spectroscopy, 54, 402–405.
——— (2000b) Vibrational spectroscopy of ferruginous smectite and nontronite. Spectrochimica Acta Part A: Molecular and biomolecular spectroscopy, 56, 2177–2189.
Gailhanou, H., Blanc, P., Rogez, J., Mikaelian, G., Kawaji, H., Olives, J., Amouric, M., Denoyel, R., Bourrelly, S., Montouillout, V., and others (2012) Thermodynamic properties of illite, smectite and beidellite by calorimetric methods: Enthalpies of formation, heat capacities, entropies and Gibbs free energies of formation. Geochimica et Cosmochimica Acta, 89, 279–301.
Gainey, S.R., Hausrath, E.M., Adcock, C.T., Tschauner, O., Hurowitz, J.A., Ehlmann, B.L., Xiao, Y., and Bartlett, C.L. (2017) Clay mineral formation under oxidized conditions and implications for paleoenvironments and organic preservation on Mars. Nature Communications, 8, 1–7.
Gates, W.P. (2005) Infrared spectroscopy and the chemistry of dioctahedral smectites. In J.T. Kloprogge, Ed., CMS Workshop Lectures Vol. 13. Clay Minerals Society.
Gates, W.P., Petit, S., and Madejová, J. (2017) Chapter 7—Applications of NIR/MIR to determine site occupancy in smectites. In W.P. Gates, J.T. Kloprogge, J. Madejová, and F. Bergaya, Eds., Developments in Clay Science, 8, pp. 200–221. Elsevier.
Gaudin, A., Petit, S., Rose, J., Martin, F., Decarreau, A., Noack, Y., and Borschneck, D. (2004) The accurate crystal chemistry of ferric smectites from the lateritic nickel ore of Murrin Murrin (Western Australia). II. Spectroscopic (IR and EXAFS) approaches. Clay Minerals, 39, 453–467.
Grauby, O., Petit, S., Decarreau, A., and Baronnet, A. (1993) The beidellite-saponite series: An experimental approach. European Journal of Mineralogy, 623–636.
——— (1994) The nontronite-saponite series: An experimental approach. European Journal of Mineralogy, 6, 99–112.
Greenberger, R.N., Mustard, J.F., Kumar, P.S., Dyar, M.D., Breves, E.A., and Sklute, E.C. (2012) Low temperature aqueous alteration of basalt: Mineral assemblages of Deccan basalts and implications for Mars. Journal of Geophysical Research: Planets, 117, E00J12.
Grotzinger, J.P., Sumner, D.Y., Kah, L.C., Stack, K., Gupta, S., Edgar, L., Rubin, D., Lewis, K., Schieber, J., Mangold, N., and others (2014) A habitable fluvio-lacustrine environment at Yellowknife Bay, Gale Crater, Mars. Science, 343.
Guven, N. (1988) Smectites. Reviews in Mineralogy and Geochemistry, 19, 497–559.
Hadi, J., Tournassat, C., Ignatiadis, I., Greneche, J.M., and Charlet, L. (2013) Modelling CEC variations versus structural iron reduction levels in dioctahedral smectites. Existing approaches, new data and model refinements. Journal of Colloid and Interface Science, 407, 397–409.
Hamilton, V.E., Simon, A.A., Christensen, P.R., Reuter, D.C., Clark, B.E., Barucci, M.A., Bowles, N.E., and others. (2019) Evidence for widespread hydrated minerals on Asteroid (101955) Bennu. Nature Astronomy, 3 (4), 332–40. https://doi.org/10.1038/s41550-019-0722-2
Hunt, G. (1977) Spectral signatures of particulate minerals in the visible and near infrared. GEOPHYSICS, 42, 501–513.
Inoue, A., and Utada, M. (1991) Smectite-to-chlorite transformation in thermally metamorphosed volcanoclastic rocks in the Kamikita area, northern Honshu, Japan. American Mineralogist, 76, 628–640.
Jones, E., Oliphant, T., and Peterson, P. (2001) SciPy: Open source scientific tools for Python. Available at: http://www.scipy.org/, accessed July 20, 2018
Keeling, J.L., Raven, M.D., and Gates, W.P. (2000) Geology and characterization of two hydrothermal nontronites from weathered metamorphic rocks at the Uley graphite mine, South Australia. Clays and Clay Minerals, 48, 537–548.
Kimbara, K., and Honda, S. (1975) An iron-rich saponite-like mineral found in the Moriyama volcanic rocks, Gojome, Akita Prefecture, Japan. Bulletin of the Geological Survey of Japan, 26, 37–40.
Kodama, H., Dekimpe, C.R., and Dejou, J. (1988) Ferrian saponite in a gabbro saprolite at Mont Mégantic, Quebec. Clays and Clay Minerals, 36, 102–110.
Kohyama, N., Shimoda, S., and Sudo, T. (1973) Iron-rich saponite (ferrous and ferric forms). Clays and Clay Minerals, 21, 229–237.
Koster, H.M., Ehrlicher, U., Gilg, H.A., Jordan, R., Murad, E., and Onnich, K. (1999) Mineralogical and chemical characteristics of five nontronites and Fe-rich smectites. Clay Minerals, 34, 579–599.
Lajarige, C., Petit, S., Augas, C., and Decarreau, A. (1998) Stabilisation of Fe^{2+} ions in synthetic ferroan smectites. Comptes Rendus de l'Academie des Sciences – Series IIA – Earth and Planetary Science, 12, 789–794.
Madejová, J., and Pálková, H. (2017) Chapter 13—NIR Contribution to The Study of Modified Clay Minerals. In W.P. Gates, J.T. Kloprogge, J. Madejová, and F. Bergaya, Eds., Developments in Clay Science Vol. 8, pp. 447–481. Elsevier.
Madejová, J., Komadel, P., and Čičel, B. (1994) Infrared study of octahedral site populations in smectites. Clay Minerals, 29, 319–326.
Madejová, J., Bujdák, J., Petit, S., and Komadel, P. (2000) Effects of chemical composition and temperature of heating on the infrared spectra of Li-saturated dioctahedral smectites. (II) Near-infrared region. Clay Minerals, 35, 753–761.
Madejová, J., Janek, M., Komadel, P., Herbert, H.-J., and Moog, H.C. (2002) FTIR analyses of water in MX-80 bentonite compacted from high salinary salt solution systems. Applied Clay Science, 20, 255–271.
Manceau, A., Drits, V.A., Lanson, B., Chateigner, D., Wu, J., Huo, D., Gates, W.P., and Stucki, J.W. (2000a) Oxidation-reduction mechanism of iron in dioctahedral smectites: II. Crystal chemistry of reduced Garfield nontronite. American Mineralogist, 85, 153–172.
Manceau, A., Lanson, B., Drits, V.A., Chateigner, D., Gates, W.P., Wu, J., Huo, D., and Stucki, J.W. (2000b) Oxidation-reduction mechanism of iron in dioctahedral smectites: I. Crystal chemistry of oxidized reference nontronites. American Mineralogist, 85, 133–152.
McCollom, T.M., Ehlmann, B.L., Wang, A., Hynek, B.M., Moskowitz, B., and Berquó, T.S. (2014) Detection of iron substitution in natroalunite-natrojarosite solid solutions and potential implications for Mars. American Mineralogist, 99, 948–964.
Mermut, A.R., and Cano, A.F. (2001) Baseline studies of The Clay Minerals Society source clays: Chemical analyses of major elements. Clays and Clay Minerals, 49, 381–386.
Michalski, J.R., Kraft, M.D., Sharp, T.G., Williams, L.B., and Christensen, P.R. (2005) Mineralogical constraints on the high-silica martian surface component observed by TES. Icarus, 174, 161–177.

Michalski, J.R., Kraft, M.D., Sharp, T.G., Williams, L.B., and Christensen, P.R. (2006) Emission spectroscopy of clay minerals and evidence for poorly crystalline aluminosilicates on Mars from thermal emission spectrometer data. Journal of Geophysical Research: Planets, 111, E03004.

Michalski, J., Poulet, F., Bibring, J.-P., and Mangold, N. (2010) Analysis of phyllosilicate deposits in the Nili Fossae region of Mars: Comparison of TES and OMEGA data. Icarus, 206, 269–289.

Michalski, J.R., Cuadros, J., Bishop, J.L., Dyar, M.D., Dekov, V., and Fiore, S. (2015) Constraints on the crystal-chemistry of Fe/Mg-rich smectitic clays on Mars and links to global alteration trends. Earth and Planetary Science Letters, 427, 215–225.

Moore, D.M., and Reynolds, R.C. (1997) X-ray diffraction and the identification and analysis of clay minerals. Oxford University Press, New York.

Morgan, J., and Warren, B.E. (1938) X-ray analysis of the structure of water. The Journal of Chemical Physics, 6, 666–673.

Morris, R.V., Klingelhöfer, G., Schröder, C., Rodionov, D.S., Yen, A., Ming, D.W., Souza, P.A., de Fleischer, I., Wdowiak, T., Gellert, R., and others (2006). Mössbauer mineralogy of rock, soil, and dust at Gusev crater, Mars: Spirit's journey through weakly altered olivine basalt on the plains and pervasively altered basalt in the Columbia Hills. Journal of Geophysical Research: Planets, 111(E2). https://doi.org/10.1029/2005JE002584.

Murad, E. (1987) Mössbauer spectra of nontronites: Structural implications and characterization of associated iron oxides. Zeitschrift für Pflanzenernährung und Bodenkunde, 150, 279–285.

Murad, E., and Schwertmann, U. (1984) The influence of crystallinity on the Mössbauer spectrum of lepidocrocite. Mineralogical Magazine, 48, 507–511.

Newville, M., Stensitzki, T., Allen, D.B., and Ingargiola, A. (2014) LMFIT: Non-Linear Least-Square Minimization and Curve-Fitting for Python. Available at: https://lmfit.github.io/lmfit-py/index.html, accessed March 10, 2018.

Niu, B., and Yoshimura, T. (1996) Smectite conversion in diagenesis and low grade hydrothermal alteration from Neogene basaltic marine sediments in Niigata Basin, Japan. Clay Science, 10, 37–56.

Parthasarathy, G., Choudary, B.M., Sreedhar, B., Kunwar, A.C., and Srinivasan, R. (2003) Ferrous saponite from the Deccan Trap, India, and its application in adsorption and reduction of hexavalent chromium. American Mineralogist, 88, 1983–1988.

Petit, S., Decarreau, A., Gates, W., Andrieux, P., and Grauby, O. (2015) Hydrothermal synthesis of dioctahedral smectites: The Al-Fe^{3+} chemical series. Part II: Crystal-chemistry. Applied Clay Science, 104, 96–105.

Post, J.L. (1984) Saponite from near Ballarat, California. Clays and Clay Minerals, 32, 147–153.

Poulet, F., Bibring, J.-P., Mustard, J.F., Gendrin, A., Mangold, N., Langevin, Y., Arvidson, R.E., Gondet, B., Gomez, C., Berthé, M., and others (2005) Phyllosilicates on Mars and implications for early martian climate. Nature, 438, 623–627.

Poulet, F., Mangold, N., Loizeau, D., Bibring, J.-P., Langevin, Y., Michalski, J., and Gondet, B. (2008) Abundance of minerals in the phyllosilicate-rich units on Mars. Astronomy and Astrophysics, 487, L41–L44.

Quirico, E., Montagnac, G., Rouzaud, J.-N., Bonal, L., Bourot-Denise, M., Duber, S., and Reynard, B. (2009) Precursor and metamorphic condition effects on Raman spectra of poorly ordered carbonaceous matter in chondrites and coals. Earth and Planetary Science Letters, 287, 185–193.

Rampe, E.B., Ming, D.W., Blake, D.F., Bristow, T.F., Chipera, S.J., Grotzinger, J.P., Morris, R.V., Morrison, S.M., Vaniman, D.T., Yen, A.S., and others (2017) Mineralogy of an ancient lacustrine mudstone succession from the Murray formation, Gale crater, Mars. Earth and Planetary Science Letters, 471, 172–185.

Rivkin, A.S., Davies, J.K., Johnson, J.R., Ellison, S.L., Trilling, D.E., Brown, R.H., and Lebofsky, L.A. (2003) Hydrogen concentrations on C-class asteroids derived from remote sensing. Meteoritics and Planetary Science, 38, 1383–1398.

Rivkin, A.S., Volquardsen, E.L., and Clark, B.E. (2006) The surface composition of Ceres: Discovery of carbonates and iron-rich clays. Icarus, 185, 563–567.

Rossman, G.R. (1976) Spectroscopic and magnetic studies of ferric iron hydroxy sulfates: The series $Fe(OH)SO_4.nH_2O$ and the jarosites. American Mineralogist, 61, 398–404.

Ruff, S.W., and Christensen, P.R. (2007) Basaltic andesite, altered basalt, and a TES-based search for smectite clay minerals on Mars. Geophysical Research Letters, 34, L10204.

Sapers, H.M., Razzell Hollis, J., Bhartia, R., Beegle, L.W., Orphan, V.J., and Amend, J.P. (2019) The cell and the sum of its parts: Patterns of complexity in biosignatures as revealed by deep UV Raman spectroscopy. Frontiers in Microbiology, 10.

Schmidt, E.R., and Heystek, H. (1953) A saponite from Krugersdorp district, Transvaal. Mineralogical Magazine and Journal of the Mineralogical Society, 30, 201–210.

Schopf, J.W., Kudryavtsev, A.B., Agresti, D.G., Czaja, A.D., and Wdowiak, T.J. (2005) Raman imagery: A new approach to assess the geochemical maturity and biogenicity of permineralized Precambrian fossils. Astrobiology, 5, 333–371.

Sholes, S.F., Smith, M.L., Claire, M.W., Zahnle, K.J., and Catling, D.C. (2017) Anoxic atmospheres on Mars driven by volcanism: Implications for past environments and life. Icarus, 290, 46–62.

Socrates, G. (2004) Infrared and Raman Characteristic Group Frequencies: Tables and charts, 390 p. Wiley.

Son, B.-K., Yoshimura, T., and Fukasawa, H. (2001) Diagenesis of dioctahedral and trioctahedral smectites from alternating beds in Miocene to Pleistocene rocks of the Niigata Basin, Japan. Clays and Clay Minerals, 49, 333–346.

Suquet, H., Calle, C.D.L., and Pezerat, H. (1975) Swelling and structural organization of saponite. Clays and Clay Minerals, 23, 1–9.

Tarafder, P.K., and Thakur, R. (2013) An optimised 1,10-phenanthroline method for the determination of ferrous and ferric oxides in silicate rocks, soils and minerals. Geostandards and Geoanalytical Research, 37, 155–168.

Treiman, A.H., Morris, R.V., Agresti, D.G., Graff, T.G., Achilles, C.N., Rampe, E.B., Bristow, T.F., Blake, D.F., Vaniman, D.T., Bish, D.L., and others (2014) Ferrian saponite from the Santa Monica Mountains (California, U.S.A., Earth): Characterization as an analog for clay minerals on Mars with application to Yellowknife Bay in Gale Crater. American Mineralogist, 99, 2234–2250.

Uckert, K., Bhartia, R., and Michel, J. (2019) A semi-autonomous method to detect cosmic rays in Raman hyperspectral data sets. Applied Spectroscopy, 73, 1019–1027.

Ufer, K., Roth, G., Kleeberg, R., Stanjek, H., Dohrmann, R., and Bergmann, J. (2004) Description of X-ray powder pattern of turbostratically disordered layer structures with a Rietveld compatible approach. Zeitschrift für Kristallographie—Crystalline Materials, 219, 519–527.

Ulery, A.L., and Drees, L.R. (2008) Methods of soil analysis: Mineralogical methods. Part 5 Vol. 9. ASA-CSSA-SSSA.

van de Walt, S., Colbert, S.C., and Varoquaux, G. (2011) The NumPy array: a structure for efficient numerical computation. Computing in Science and Engineering, Institute of Electrical and Electronics Engineers, 13 (2), pp.22–30.

Van Olphen, H., and Fripiat, J.J. (1979) Data Handbook for Clay Materials and Other Non-Metallic Minerals. Pergamon Press, Oxford.

Vaniman, D.T., Bish, D.L., Ming, D.W., Bristow, T.F., Morris, R.V., Blake, D.F., Chipera, S.J., Morrison, S.M., Treiman, A.H., Rampe, E.B., and others (2013) Mineralogy of a mudstone at Yellowknife Bay, Gale Crater, Mars. Science, 1243480.

Vantelon, D., Montarges-Pelletier, E., Michot, L.J., Briois, V., Pelletier, M., and Thomas, F. (2003) Iron distribution in the octahedral sheet of dioctahedral smectites: An Fe *K*-edge X-ray absorption spectroscopy study. Physics and Chemistry of Minerals, 30, 44–53.

Wang, A., Freeman, J.J., and Jolliff, B.L. (2015) Understanding the Raman spectral features of phyllosilicates. Journal of Raman Spectroscopy, 46, 829–845.

Weir, A.H., and Greene-Kelly, R. (1962) Beidellite. American Mineralogist, 47, 137–146.

Wiens, R.C., Maurice, S., and Rull Perez, F. (2017) The SuperCam remote sensing instrument suite for the Mars 2020 rover mission: A preview. Spectroscopy, 32.

Manuscript received December 31, 2019
Manuscript accepted November 25, 2020
Manuscript handled by Sylvain Grangeon

Endnote:

[1]Deposit item AM-21-67419, Online Material. Deposit items are free to all readers and found on the MSA website, via the specific issue's Table of Contents (go to http://www.minsocam.org/MSA/AmMin/TOC/2021/Jun2021_data/Jun2021_data.html).